Heliyon 5 (2019) e01757

Contents lists available at ScienceDirect

Heliyon

journal homepage: www.heliyon.com

Numerical analysis of natural convective heat transport of copper oxide-water nanofluid flow inside a quadrilateral vessel

M.J. Uddin *, S.K. Rasel

Faculty of Science and Information Technology, Daffodil International University, Dhaka, Bangladesh

ARTICLE INFO

Keywords:
Energy
Mechanical engineering
Nanotechnology
Applied mathematics
Computational mathematics

ABSTRACT

Nanofluid based heat transfer approaches have a tremendous prospect to develop novel cost-effective cooling technologies. In response to this potential development, a problem of unsteady copper oxide-water nanofluid flow and natural convective heat transfer within a quadrilateral vessel with uniform heating of bottom wall using modified Buongiorno model are investigated. The sloping wall of the vessel is maintained at constant low temperature and the uniform thermal condition on the bottom heated wall is considered, whereas the upper horizontal wall is regarded as adiabatic. The governing equations along with boundary conditions are solved using the Galerkin finite element method. Partial differential equation solver COMSOL Multiphysics with Matlab interface is used in the simulation. The results of the present problem of a certain situation as a special case have been verified by the previously published standard numerical investigations. The flow, thermal and concentration fields, local and average Nusselt number for various pertinent parameters entered into the problem have been analyzed. The time evolutions for a steady-state solution are also examined. The results show that the adjustment factor with the optimal nanoparticle volume fraction and the thermal Rayleigh number controls the optimal heat transfer. The trapezoidal vessel having higher sloping angles with the vertical axis exhibits higher heat transfer. Heat transfer decreases rapidly in 1–10 nm size nanoparticles for a nanofluid solution.

1. Introduction

Natural convection heat transfer has wide applications in electronic and mechanical engineering systems for the purpose of cooling and heating. The perspective of energy saving during heat transfer in these systems is a crucial issue. A series of experiments have been carried out in the literature in order to enhance the heat transfer rate using conventional fluid and solid separately. Solid has higher thermal conductivity than that of fluid. As for example, the thermal conductivity of zinc oxide is higher than that of the typical fluids like water or engine oil and so on. Nowadays, buoyancy-driven nanofluids flow and heat transfer analysis within various enclosures are popular research areas in science and engineering fields. Specifically, the study of free convective incompressible nanofluids flow inside several rectangular shaped cavities appeals the scientific communities. Nanofluid is a stable mixture of conventional fluid and nanoparticles. Heat transfer enhancement using nanofluid directly depends on the nanofluid filled geometry, combinational of the base fluid and nanoparticles, high thermal conductivity, least impediment in fluid flow, longevity, stability, and homogeneity of nanoparticles (Uddin et al. [1]). Nanofluids have significant potentialities in microelectronics, pharmaceutical processes, fuel-cells, hybrid-powered engines, refrigerator, chiller and heat exchangers where heat transfer enhancement is required. It is worth mentioning that the insights of nanofluids, hybrid nanofluids flow and applicability of nanofluids can be found in the papers of Mehryan et al. [2], Chamkha et al. [3], Mehryan et al. [4], in the book by Shenoy et al. [5], Mahian et al. [6, 7], Das et al. [8], Minkowycz et al. [9] and in the review paper by Mahian et al. [10] and several others.

Appropriate modeling of convective heat transport can be ensured the utility of a particular nanofluid. Several scientists' have undertaken diverse studies discussing the convection process in the nanofluid filled trapezoidal cavity. Saleh et al. [11] studied the natural convection of water based copper and alumina nanofluids flow in a trapezoidal cavity. Their results showed that the effective heat transfer enhancement occurs for a trapezoidal cavity having an acute geometry inclined angle with a high concentration of copper nanoparticles. Soleimani et al. [12] studied natural convection heat transfer within a copper-water nanofluid filled a semi-annulus cavity. Their results showed that there is an optimum angle of turn for which the rate of heat transfer is maximum for several thermal Rayleigh numbers. Roslan et al. [13] investigated the buoyancy-driven

* Corresponding author.
E-mail address: jashim.fluidm@gmail.com (M.J. Uddin).

https://doi.org/10.1016/j.heliyon.2019.e01757
Received 24 February 2019; Received in revised form 26 March 2019; Accepted 14 May 2019

heat transfer within a nanofluid filled trapezoidal cavity with variable thermal conductivity and viscosity. They reported that the effect of the viscosity was more dominant than the thermal conductivity in heat transfer augmentation and heat transfer enhancement is not that much noticeable for using nanofluid. Mahmoudi et al. [14] have studied the natural convection heat transfer using copper-water nanofluid flow in a trapezoidal enclosure. Their results disclosed that the enhancement in average Nusselt Number occurs for a certain lower Reynolds Number whereas heat transfer declines significantly for the higher Reynolds Number. Nasrin and Parvin [15] investigated the natural convective heat transfer utilizing copper-water nanofluid in a trapezoidal enclosure and showed that the aspect ratio and the Prandtl number significantly enhance the nanofluid flow and heat transfer. In addition, they recommended a correlation of average Nusselt number in terms of Prandtl number and cavity aspect ratio. Bondareva et al. [16] studied unsteady natural convection in a right-angled trapezoidal cavity filled with nanofluid using Buongiorno's model. Their results showed that the pivotal parameters of the problem substantively stimulate the flow field as well as the heat and mass transfer. Aghaei et al. [17] studied the effects of magnetic field and entropy generation on mixed convection utilizing nanofluid in a trapezoidal enclosure. They found that the magnetic field shrinks the convective heat transfer and flow strength of nanofluid. The insignificant measurement of entropy generation notices for frictions whereas noteworthy entropy generation takes place for an irreversible state of heat transfer. Selimefendigil et al. [18] investigated the natural convection and heat generation in a nanofluid filled entrapped trapezoidal cavities under an influence of the magnetic field. Their study reports that the mean heat transfer decreases as the magnetic field parameter increases for higher thermal Rayleigh number. Alipour et al. [19] studied the influence of T-semi attached rib on turbulent flow and heat transfer parameters of a silver-water nanofluid with different volume fractions in a three-dimensional trapezoidal microchannel. They showed that the heat transfer coefficient is increased as the Reynolds number and volume fraction of solid nanoparticle are increased. Esfe et al. [20] studied natural convection in a trapezoidal enclosure filled with carbon nanotube and water-ethylene glycol nanofluid. Their results showed that at a low Rayleigh number, the average Nusselt number is decreased when the inclination angle or aspect ratio is increased. Job and Gunakala [21] studied unsteady natural convective alumina-water and single-walled carbon nanotube-water nanofluids flow in a curly trapezoidal cavity with Joule viscous dissipation. They reported that the heat transfer rate at the wavy heated wall is decreased for alumina-water nanofluid whereas it is increased for carbon nanotube-water nanofluid. There are also some notable numerical investigations are worthwhile in the literature includes Job et al. [22], Arefmanesh et al. [23], Selimefendigil and Öztop [24] and Sheremet et al. [25] and Miroshnichenko et al. [26].

The objective of the present work is to observe the mechanisms as well as the enhancement of heat transfer in a quadrilateral vessel for copper oxide (CuO)-water nanofluid using a nonhomogeneous dynamic model. The reason for selecting a quadrilateral vessel is that it has wide applications in the field of nuclear, civil, mechanical and architectural engineering. Especially, to use as a fluid-filled solar thermal collector, security tool and electrical device, nanofluid filled trapezoidal cavity have a comprehensive prospect. Investigating heat transfer in different enclosures are necessary for selecting an appropriate heat transfer tool in engineering application. Hence, analysis of the flow dynamics of nanofluids and heat transfer mechanisms within a quadrilateral vessel can be a contribution in the field of electrical and mechanical engineering. Recently, Job et al. [22] and Al-Weheibi et al. [27] studied the effect of solid volume fraction in a trapezoidal shape enclosure filled with several water-based nanofluids. In their study, Brownian motion, thermophoresis and magnetic field effect, as well as the nanofluid concentration equation, have been neglected. So, in order to predict the accurate result, these effects must be considered in the modeling. As per the authors' knowledge, the literature review revealed that using uniform heating of bottom wall taking into the nonhomogeneous dynamic model in a quadrilateral vessel filled with water-based copper-oxide nanofluid has not been studied yet. The study has been carried out numerically using the Galerkin finite element method and the related results have been shown graphically for copper oxide (CuO)-water nanofluid in the form of streamlines, isotherms, and isoconcentrations. Moreover, the heat transfer distributions and average heat transfer have been displayed in various graphical forms considering practical applications. Subsequently, the quadrilateral vessel presented in this paper can have an excessive usage in numerous areas of engineering, the numerical analysis demonstrated can benefit to encourage the practice of energy, exclusively in the electrical and mechanical engineering.

2. Model

A physical model of the investigation is shown in Fig. 1 where the Cartesian coordinates are x and y. The length and height of the quadrilateral vessel are L. The lower left corner of the vessel is placed at the origin where the bottom wall of the vessel is on the x-direction and the y-axis is normal to it. Based on the vessel's sloping angle(φ) with y-axis, three different shapes of a quadrilateral vessel are considered: case-1: $\varphi = 0^{\circ}$, case-2: $\varphi = 9^{\circ}$ and case-3: $\varphi = 15.75^{\circ}$. The wall conditions are considered from practical applications. Based on the real functional conditions in various heat exchangers, the horizontal upper wall is modeled as adiabatic assuming no heat transfer for this boundary. The temperature of the left and right inclined walls of the vessel is low as heat goes through it and demonstrated as $T = T_C$, whereas the bottom wall is uniformly heated and modeled as $T = T_h$. Under all situations $T_h > T_C$ is maintained. Primarily, it is assumed that nanofluid concentration is kept at low concentration C_C while for $t > 0$, C_h is assumed in the entire domain so that $C_h > C_C$. No-slip boundary conditions where zero velocities at all walls are considered. In this modeling, the effects of thermophoresis, Brownian diffusion, and acceleration due to gravity are included whereas effects of chemical reactions, thermal radiation, and magnetic field are not considered. We have also assumed that the base fluid and solid nanoparticles are in a thermal equilibrium state.

The mathematical equations of the present problem are the modified version of the principal equations of Buongiorno [28]. These equations are derived for a new mass flux equation (see Uddin and Rahman [29]) to use the nanoparticle volume fraction as constant, the effect of the diameter of the nanoparticle, the thermal properties of nanofluid and the thermophysical correlations accurately. The concentrations equations are rewritten as the molar concentration of nanofluid to understand the level of the concentration which produces the state of the nanoparticle in the solution for the effects of the different related parameters. As per the author's knowledge, the problem of natural convective heat transfer on copper oxide-water nanofluid filled quadrilateral vessel taking into account the modified equations of Buongiorno's model along with uniform thermal boundary conditions are not studied yet. Hence, the obtained results of the present investigations are innovative. Let us consider the two-dimensional unsteady incompressible laminar natural convective copper oxide-water nanofluid flow within the quadrilateral vessel. The nanoparticles are assumed as the species of the base fluid because they are compatible with molecules in size and can be easily fluidized. The small particles act like the molecules of the base fluid. Nonhomogeneous state of the mixture occurs for the dynamic effects of the nanoparticles such as the Brownian and thermophoretic diffusions due to the strong temperature differences within the nanofluid. In Cartesian coordinates, the governing equations (Uddin and Rahman [29]) of nanofluid are:

$$\frac{\partial u}{\partial x} + \frac{\partial v}{\partial y} = 0 \tag{1}$$

$$\rho_{nf}\left[\frac{\partial u}{\partial t} + u\frac{\partial u}{\partial x} + v\frac{\partial u}{\partial y}\right] = -\frac{\partial p}{\partial x} + \mu_{nf}\left(\frac{\partial^2 u}{\partial x^2} + \frac{\partial^2 u}{\partial y^2}\right) \tag{2}$$

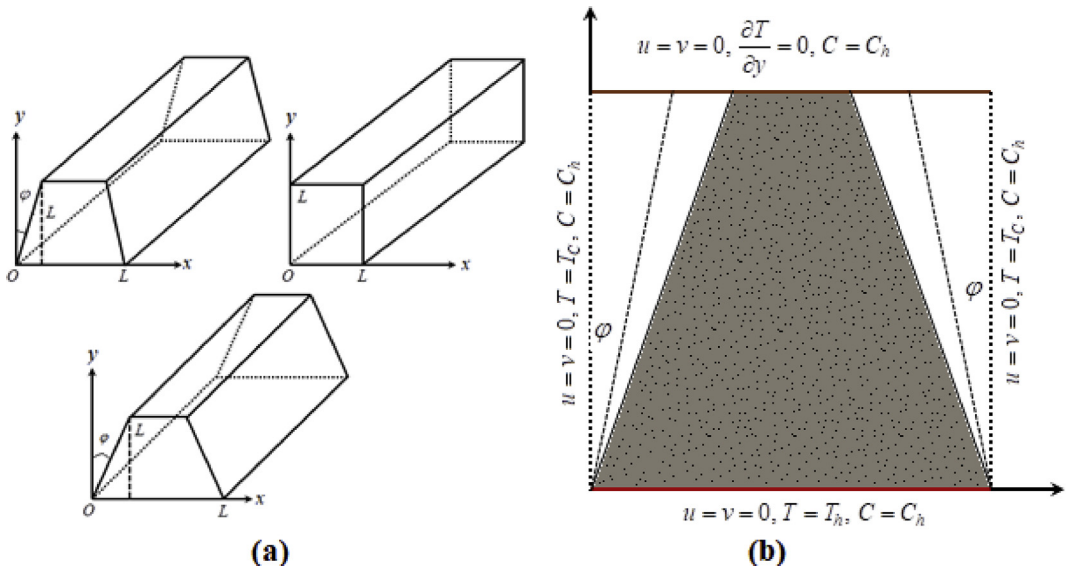

Fig. 1. The diagram of the physical system of the problem, (a) 3D geometry, (b) two-dimensional cross-section.

$$\rho_{nf}\left[\frac{\partial v}{\partial t}+u\frac{\partial v}{\partial x}+v\frac{\partial v}{\partial y}\right]=-\frac{\partial p}{\partial y}+\mu_{nf}\left(\frac{\partial^2 v}{\partial x^2}+\frac{\partial^2 v}{\partial y^2}\right)+(\rho\beta)_{nf}g(T-T_c)+\left(\rho\beta^*\right)_{nf}g(C-C_c) \tag{3}$$

$$\frac{\partial T}{\partial t}+u\frac{\partial T}{\partial x}+v\frac{\partial T}{\partial y}=\alpha_{nf}\left(\frac{\partial^2 T}{\partial x^2}+\frac{\partial^2 T}{\partial y^2}\right)+\frac{D_B}{C}\left(\frac{\partial C}{\partial x}\frac{\partial T}{\partial x}+\frac{\partial C}{\partial y}\frac{\partial T}{\partial y}\right)+\frac{D_T}{T}\left[\left(\frac{\partial T}{\partial x}\right)^2+\left(\frac{\partial T}{\partial y}\right)^2\right] \tag{4}$$

$$\frac{\partial C}{\partial t}+u\frac{\partial C}{\partial x}+v\frac{\partial C}{\partial y}=D_B\left(\frac{\partial^2 C}{\partial x^2}+\frac{\partial^2 C}{\partial y^2}\right)+\frac{C\,D_T}{T}\left(\frac{\partial^2 T}{\partial x^2}+\frac{\partial^2 T}{\partial y^2}\right)+\frac{D_T}{T}\left(\frac{\partial C}{\partial x}\frac{\partial T}{\partial x}+\frac{\partial C}{\partial y}\frac{\partial T}{\partial y}\right) \tag{5}$$

where two-dimensional Eqs. (1), (2), (3), (4), and (5) are the continuity, momentum in *x*- and *y*- directions, energy, and concentration equations respectively. The dimensional velocity components along x and y co-ordinates are u and v respectively. Here, ρ_{nf} μ_{nf} C_C, p, g, T_C, $(\rho c_p)_{nf}$, α_{nf}, $(\rho\beta)_{nf}$ and $(\rho\beta^*)_{nf}$ are the density, dynamic viscosity, reference concentration, pressure, acceleration due to gravity, reference temperature, heat capacity, thermal diffusivity, volumetric thermal expansion and volumetric mass expansion of nanofluid respectively. Note that volumetric mass expansion happens due to diverse concentration differences within nanofluid inside the enclosure. Here the subscripts *p*, *nf* and *bf* represents solid particle, nanofluid, and base fluid respectively. The Eqs. (4) and (5) are the reformed energy and molar concentration equations which are the modified versions of Buongiorno's energy and nanoparticle volume fraction equations. The coefficients of Eqs. (4) and (5) come out for the mass flux equation of nanofluid where T, C, D_B and D_T are dimensional temperature, concentration, Brownian diffusion coefficient, and thermophoretic diffusion coefficient of nanofluid respectively. The following correlations of the thermophysical properties of nanofluids are used in the simulation (Xuan et al. [30], Tiwari and Das [31], Uddin et al. [32] and Uddin [33]):

$$\kappa_{nf}=\frac{-2\phi(\kappa_{bf}-\kappa_p)+2\kappa_{bf}+\kappa_p}{\phi(\kappa_{bf}-\kappa_p)+2\kappa_{bf}+\kappa_p}\kappa_{bf}+\frac{\rho_p c_p \phi}{2D_T^{\prime}}\left(\frac{2k_B T_C D_T}{3\pi\mu_{nf}d_p}\right)^{\frac{1}{2}} \tag{6}$$

$$\rho_{nf}=(1-\phi)\rho_{bf}+\phi\rho_p \tag{7}$$

$$\mu_{nf}=\mu_{bf}(1-\phi)^{-2.5} \tag{8}$$

$$\left(\rho\beta^*\right)_{nf}=(1-\phi)\left(\rho\beta^*\right)_{bf}+\phi\left(\rho\beta^*\right)_p \tag{9}$$

$$(\rho\beta)_{nf}=(1-\phi)(\rho\beta)_{bf}+\phi(\rho\beta)_p \tag{10}$$

$$\left(\rho c_p\right)_{nf}=(1-\phi)\left(\rho c_p\right)_{bf}+\phi\left(\rho c_p\right)_p \tag{11}$$

$$\alpha_{nf}=\kappa_{nf}\left(\rho c_p\right)_{nf}^{-1} \tag{12}$$

$$D_T=0.126\frac{\kappa_{nf}}{\kappa_{bf}}\frac{\hbar\beta_{bf}\mu_{nf}}{\rho_{nf}} \tag{13}$$

$$D_B=\frac{k_B T_C}{3\pi\mu_{nf}d_p} \tag{14}$$

Table 1
Thermophysical properties of base fluids and materials at room temperature.

Items (bf, p)	(c_p) $(\mathrm{Jkg^{-1}K^{-1}})$	ρ $(\mathrm{kg\ m^{-3}})$	κ $(\mathrm{W\,m^{-1}K^{-1}})$	μ $(\mathrm{kg\,m^{-1}\ s^{-1}})$	β $(\mathrm{K^{-1}})$
water	4179	997.1	0.613	0.001003	21×10^{-5}
CuO	531.8	6320	76.5	–	1.8×10^{-5}

where κ_{nf}, μ_{bf},c_p, ϕ, d_p, k_B, β_{bf}, β^*_{bf} and D^{ϵ}_T are the thermal conductivity of nanofluid, the viscosity of the base fluid, specific heat, nanoparticle volume fraction, the diameter of nanoparticle, Boltzmann constant, thermal expansion of the bulk fluid, mass expansion of base fluid and the numeric value of $\sqrt{D_T}$ respectively. The symbol λ is the correction factor used to measure the thermal conductivity of nanofluid (Uddin et al. [1], Uddin and Rahman [29]) depends on solid particle size in the mixture as

$$\lambda = -0.0002 d_p + 0.1537 \tag{15}$$

The numerical values of Eqs. (6), (7), (8), 9 (10), (11), (12), 13) (14) and (15) are obtained using the thermophysical properties of the nanoparticle and conventional base fluid shown in Table 1.

The appropriate initial and boundary conditions for the present problem along with the above-stated model are as follows:

$$\text{For } t = 0, \text{ entire domain: } u = v = 0,\ T = T_C,\ C = C_C,\ p = 0 \tag{16}$$

For $t > 0$,

$$\text{On the horizontal wall: } u = v = 0,\ T = T_h,\ C = C_h \quad \forall\, y = 0,\ 0 \le x \le L \tag{17}$$

On the vertical wall:

$$u = v = 0,\ T = T_C,\ C = C_h \quad \forall\, x\cos(\varphi) - y\sin(\varphi) = 0,\ 0 \le y \le L \tag{18}$$

$$u = v = 0,\ T = T_C,\ C = C_h \quad \forall\, x\cos(\varphi) + y\sin(\varphi) = L\cos(\varphi),\ 0 \le y \le L \tag{19}$$

$$\text{On the upper wall: } u = v = 0,\ \frac{\partial T}{\partial y} = 0,\ C = C_h \quad \forall\, y = L,\ \tan(\varphi) \le x \le L - \tan(\varphi) \tag{20}$$

It is noted that, physically, there is no concentration within the rigid boundaries of the geometry. The concentration boundary conditions are adopted to find the solutions of the highly nonlinear governing equations. The zero concentration boundary conditions on the walls produce the singularities. In this context, to understand the concentration levels in the entire vessel, the nonzero, as well as the maximum concentration boundary condition, C_h at all walls, are applied.

A nondimensional analysis is the customary study of fluid mechanics. To describe several transport mechanisms in nanofluids, it is meaningful to make the conservation equations into non-dimensional form. The advantages of non-dimensionalization are available in the literature. Non-dimensionalization provides the sovereignty to scrutinize a few systems regardless of their material belongings. One can easily recognize the regulatory flow parameters of the system using the method of dimensionless. It is also possible in this way to make a sweeping statement of the magnitude and profile of the geometry as well as to get insight into the physical problem which are the essentials in the investigation. These aims can be achieved through the appropriate choice of scales. As a scale of distance, we choose the length of the cavity of the region under consideration measured along the x-axis. Thus, in order to reduce the dimensionless form of the governing Eqs. (1), (2), (3), (4), and (5) with boundary conditions, Eqs. (16), (17), (18), (19), and (20), we incorporate the following dimensionless variables

$$\xi = \frac{\alpha_{bf} t}{L^2},\ X = \frac{x}{L},\ V = \frac{vL}{\alpha_{bf}},\ U = \frac{uL}{\alpha_{bf}},\ Y = \frac{y}{L},\ P = \frac{pL^2}{\rho_{bf}\alpha_{bf}^2},\ \theta = \frac{T - T_C}{\Delta T},\ \Phi = \frac{C - C_C}{\Delta C} \tag{21}$$

where, ρ_{bf} and α_{bf}, L, $\Delta C = C_h - C_C$, $\Delta T = T_h - T_C$, C_C and T_C are the density and thermal diffusivity of the base fluid, geometry reference length, concentration difference, temperature difference, nominal concentration and reference temperature within nanofluid, respectively. We have assumed that the temperature differences occurred within nanofluid are significantly smaller than the applied temperature. Also, the concentration differences due to temperature variations are nominal than the reference concentration inside the nanofluid filled enclosure. That means $(\Delta C/C_C) << 1$ and $(\Delta T/T_C) << 1$. Considering the constant properties of nanofluid and using relations given by Eq. (21) into Eqs. (1), (2), (3), (4), and (5), the dimensionless governing equations of nanofluid flow can be expressed in the following form:

$$\frac{\partial U}{\partial X} + \frac{\partial V}{\partial Y} = 0 \tag{22}$$

$$-\frac{\rho_{bf}}{\rho_{nf}}\frac{\partial P}{\partial X} + \frac{\mathrm{Pr}\,\mu_{nf}}{\nu_{bf}\rho_{nf}}\left(\frac{\partial^2 U}{\partial X^2} + \frac{\partial^2 U}{\partial Y^2}\right) = \frac{\partial U}{\partial \xi} + U\frac{\partial U}{\partial X} + V\frac{\partial U}{\partial Y} \tag{23}$$

$$-\frac{\rho_{bf}}{\rho_{nf}}\frac{\partial P}{\partial Y} + \frac{\mu_{nf}}{\nu_{bf}\rho_{nf}}\mathrm{Pr}\left(\frac{\partial^2 V}{\partial X^2} + \frac{\partial^2 V}{\partial Y^2}\right) + \frac{(\rho\beta)_{nf}}{\beta_{bf}\rho_{nf}}Ra_T\mathrm{Pr}\theta + Ra_C\mathrm{Pr}\Phi = \frac{\partial V}{\partial \xi} + U\frac{\partial V}{\partial X} + V\frac{\partial V}{\partial Y} \tag{24}$$

$$\frac{\alpha_{nf}}{\alpha_{bf}}\left(\frac{\partial^2 \theta}{\partial X^2} + \frac{\partial^2 \theta}{\partial Y^2}\right) + \frac{1}{Le}\left(\frac{\partial \Phi}{\partial X}\frac{\partial \theta}{\partial X} + \frac{\partial \Phi}{\partial Y}\frac{\partial \theta}{\partial Y}\right) + \frac{\mathrm{Pr}N_{TBT}}{Sc}\left(\left(\frac{\partial \theta}{\partial X}\right)^2 + \left(\frac{\partial \theta}{\partial Y}\right)^2\right) = \frac{\partial \theta}{\partial \xi} + U\frac{\partial \theta}{\partial x} + V\frac{\partial \theta}{\partial y} \tag{25}$$

$$\frac{\mathrm{Pr}}{Sc}\left(\frac{\partial^2 \Phi}{\partial X^2} + \frac{\partial^2 \Phi}{\partial Y^2}\right) + \frac{\mathrm{Pr}}{Sc}\left[N_{TBTC}\left(\frac{\partial^2 \theta}{\partial X^2} + \frac{\partial^2 \theta}{\partial Y^2}\right) + N_{TBT}\left(\frac{\partial \Phi}{\partial X}\frac{\partial \theta}{\partial X} + \frac{\partial \Phi}{\partial Y}\frac{\partial \theta}{\partial Y}\right)\right] = \frac{\partial \Phi}{\partial \xi} + U\frac{\partial \Phi}{\partial X} + V\frac{\partial \Phi}{\partial Y} \tag{26}$$

where Eqs. (1), (2), (3), (4), and (5) are the dimensionless continuity, momentum in X- and Y- coordinates, energy, and concentration equations respectively. In addition, ξ, X and Y, U and V, P, θ and Φ are the dimensionless time, coordinates, velocities along X and Y directions, pressure, temperature, and concentration respectively. The nondimensional parameters usually introduced in dimensionless principal Eqs. (22), (23), (24), (25), and (26) by the nondimensional variables (see Eq. (21)) and due to the considered relations $(\Delta T/T_C) << 1$ and $(\Delta C/C_C) << 1$, where the reference temperature and molar reference concentration appeared. The dimensionless parameters are as follows:$Ra_C = \frac{L^3 g \Delta C}{\nu_{bf}\alpha_{bf}}\frac{(\rho\beta^*)_{nf}}{\rho_{nf}}$ is the local solutal Rayleigh number, $Ra_T = \frac{L^3\beta_{bf} g \Delta T}{\nu_{bf}\alpha_{bf}}$ is the local thermal Rayleigh number, $\mathrm{Pr} = \frac{\nu_{bf}}{\alpha_{bf}}$, is the Prandtl number, $Le = \frac{\kappa_{bf} C_C}{(\rho c_p)_{bf} D_B \Delta C}$ is the modified Lewis number, $N_{TBTC} = \frac{D_T}{D_B}\frac{\Delta T}{\Delta C}\frac{C_C}{T_C}$ is the dynamic diffusion parameter, $N_{TBT} = \frac{D_T}{D_B}\frac{\Delta T}{T_C}$ is the dynamic thermo-diffusion parameter and $Sc = \frac{\mu_{bf}}{\rho_{bf} D_B}$ is the Schmidt number.

The initial and boundary conditions in dimensionless form for the present problem can be written as:

$$\text{For } \xi = 0, \text{ entire domain: } U = V = 0,\quad \theta = 0,\quad \Phi = 0,\ \mathrm{P} = 0 \tag{27}$$

For $\xi > 0$,

$$\text{On horizontal base wall: } U = 0,\quad V = 0,\quad \theta = 1 \quad \forall\, Y = 0,\ 0 \le X \le 1 \tag{28}$$

On the inclined wall:

$$U = 0,\quad V = 0,\quad \theta = 0,\quad \forall\, X\cos(\varphi) - Y\sin(\varphi) = 0,\ 0 \le Y \le 1 \tag{29}$$

$$U = 0,\quad V = 0,\quad \theta = 0,\quad \forall\, X\cos(\varphi) + Y\sin(\varphi) = \cos(\varphi),\ 0 \le Y \le 1 \tag{30}$$

Upper wall of trapezium: $U=0, \quad V=0, \quad \dfrac{\partial\theta}{\partial Y}=0, \quad \forall \quad Y=1, \ \tan(\varphi) \leq X \leq 1-\tan(\varphi)$ (31)

The heat transfer distribution is represented by the local Nusselt number (Nu_L) for nanofluid can be written as

$$Nu_L = -\frac{\kappa_{nf}}{\kappa_{bf}}\frac{\partial\theta}{\partial Y} \tag{32}$$

and at the bottom heated wall, the average Nusselt number (Nu_{av}) is expressed as

$$Nu_{av} = -\frac{\kappa_{nf}}{\kappa_{bf}}\int_0^1 \frac{\partial\theta}{\partial Y}\,dX \tag{33}$$

The fluid motion is represented by the stream function (ψ) which has been defined from the components of velocity U and V. Their relations are given by

$$U=\frac{\partial\psi}{\partial Y}, \quad V=-\frac{\partial\psi}{\partial X} \tag{34}$$

Eqs. (32) and (33) are used calculating the heat transfer distribution and the average heat transfer respectively. Also, Eq. (34) is applied to the governing Eqs. (1), (2), (3), (4), and (5) analyzing the flow field in terms of the streamlines.

3. Methodology

With the Eqs. (27), (28), (29), (30), and (31), the governing dimensionless Eqs. (22), (23), (24), (25), and (26) have been solved by Galerkin weighted residual scheme of finite element method (FEM) whose details are well analyzed by Zienkiewicz et al. [34] and Codina [35]. Uddin and Rahman [36] have studied the step by step finite element procedures on the governing equations of the present problem. In this study, all the necessary calculations have been performed to understand the finite element method over the Eqs. (22), (23), (24), (25), and (26) and the boundaries restriction, Eqs. (27), (28), (29), (30), and (31). Fixed non-uniform triangular elements are constructed from the geometrical domain in this method. Finite element equations are developed using a six-node triangular element where six nodes are connected to velocities, concentration, and temperature. In this case, only corner nodes of the element are related to pressure. The pressure gradients are matching between the momentum equations for continuity requirement and a lower order multinomial has been chosen for the continuity equation. Uniform pressure is considered with a linear element whereas it is noncontinuous between elements. Then, the Galerkin weighted residual technique is employed where the governing equations are changed to a system of integral equations. The exact integration formula is directly applied to each term of the integral equations. Then, to adjust the nonlinear system of arithmetical equations, the proposed wall conditions are executed. The set of general nonlinear arithmetical equations are resolved in the arrangement of a matrix. Newton-Raphson iteration technique and Euler backward scheme are used to find the solutions of the global matrix. A partial differential equation solver with MATLAB interface is employed for the output of the problem. The convergence criterion of the numerical solutions along with error estimation has been set to $\left|\mathbf{M}^{m+1}-\mathbf{M}^{m}\right| \leq 10^{-5}$, where $\mathbf{M}$ is the general dependent variable (U, V, θ, Φ) and m is the number of iteration.

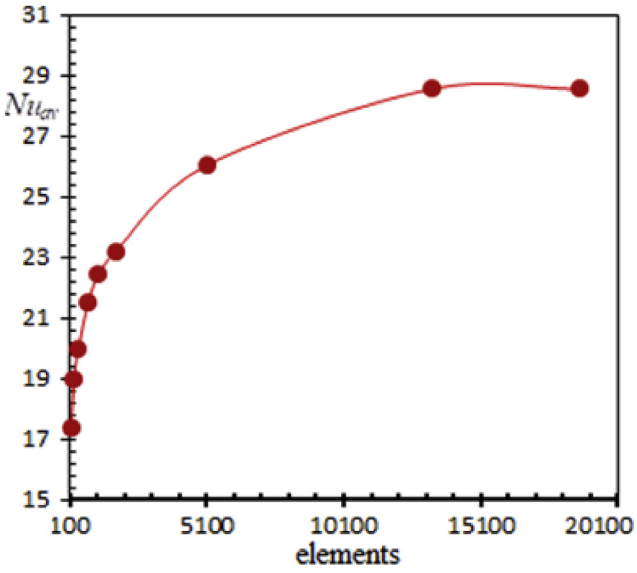

Fig. 2. Grid refinement test.

The grid independence is one of the required processes before result generation of the problem. The grid generation is a technique to divide a domain into a set of subdomains, termed finite element. The variables are calculated at the discrete locations defined by the numerical grid. It is basically a discrete representation of the geometric domain on which the problem is to be solved. Independence over the number of grids of the geometry is one of the important analysis of the simulation. In the present work, a widespread mesh testing procedure has been followed in order to guarantee a grid-independent solution for a copper oxide-water nanofluid for the fixed value $\phi = 0.05$, $d_p = 10$ nm, $Ra_C = 10^4$, $Ra_T = 10^6$, $n = 3$, at $\xi = 1$. Here, n is a spherical shaped nanoparticle. Within the resolution field, we have examined six different non-uniform grid systems with 151, 268, 418, 778, 1140, 1773, 5120 13277 and 18719 number of elements for the geometry of case-3 where the sloping angle is $\varphi = 15.75^{\circ}$. For the abovementioned elements, to develop an understanding of the grid fineness, a numerical design is executed for a specific key in terms of average Nusselt number (Nu_{av}) at the bottom heated wall as shown in Fig. 2. A small difference is observed between the scale of average Nusselt number for elements 13277 and 18719 respectively. Thus, in order to meet the grid independence study, 13277 elements are used in the numerical experiment. We have also checked the grids independency study for the quadrilateral vessel having $\varphi = 9^{\circ}$ and $\varphi = 0^{\circ}$(square). We have found that 14906 elements and 17038 elements meet the grids independency for case-2 having $\varphi = 9^{\circ}$ and case-1 having $\varphi = 0^{\circ}$ respectively.

The code validations are also imperative practices in the computa-

Table 2
Comparison of the present data (Nu_{ave}) with those of Ghasemi et al. [37] De Vahl Davis [38] and Wan et al. [39] for different values of Ra_T and ϕ while $Ra_C = 0$, $Ha = 30$, $\gamma = 0^{\circ}$, $Le^{-1} = 0$ and $N_{TBT} = 0$.

$\phi = 0$					$\phi = 0.02$	
Ra_T	Ghasemi et al. [37]	De Vahl Davis [38]	Wan et al. [39]	Present study	Ghasemi et al. [37]	Present study
10^3	1.002	1.118	1.117	1.014	1.060	1.210
10^4	1.183	2.238	2.254	1.289	1.212	1.334
10^5	3.150	4.509	4.598	3.868	3.138	3.351
10^6	7.907	4.509	8.976	8.601	7.979	9.989
10^7	16.929	-	-	17.622	17.197	18.230

tional dynamics after the grid independence study. Present numerical code is verified by comparing the data in steady case of Ghasemi et al. [37], De Vahl Davis [38] and Wan et al. [39]. Ghasemi et al. [37] have studied two-dimensional natural convection flow in a square enclosure filled with water-Al_2O_3 nanofluid in the presence of the magnetic field. In this case, present code has been transferred for the alumina-water nanofluid filled square enclosure. The nanofluid concentration equation of our study is not considered. The hydromagnetic field parameter ($Ha = 30$) with its inclination angle ($\gamma = 0^{\circ}$) are also deliberated with the momentum equations to make a similar study with those of Ghasemi et al. [37]. In a special case, where $Ra_C = 0$, $Le^{-1} = 0$ and $N_{TBT} = 0$, the average Nusselt number is estimated for the thermal Rayleigh number between 10^3 and 10^7, and nanoparticle volume fraction $\phi = 0$ and $\phi = 0.02$ which is shown in Table 2. An outstanding agreement is obtained by the present numerical code with those of Ghasemi et al. [37]. We have also compared the result of the present numerical code with standard numerical results of De Vahl Davis [38] and Wan et al. [39] where an air-filled square cavity and $Pr = 0.70$ are considered. The average Nusselt number for a special case where $Pr = 0.70$, $Ra_C = 0$ $Le^{-1} = 0$, $N_{TBT} = 0$, $\phi = 0$, $C = 0$ and $Ra_T = 10^3 - 10^6$ is displayed in Table 2. An excellent accord has been found in the comparison. The agreements of the comparisons motivate for the further numerical results of the present study.

4. Results and discussion

The thermophysical properties shown in Table 1 are used to determine the controlling parameters of the problem. The Prandtl number is 6.8377 for water. Let us assume some standard values used in available literatures, (Buongiorno [28], Tiwari and Das [31], Williams et al. [40], Garoosi et al. [41], Kim et al. [42], Uddin et al. [43, 44, 45, 46]) $\Delta T = 10K$, $\Delta C = 0.01$, $T_C = 300K$ $C_C = 1$, $d_p = 10$ nm, $n = 3$ and $\phi = 0.05$. Using these standard values and the values of thermophysical properties from Table 1, the physical parameters entered into the governing equations are obtained as follows: $Le = 3.82 \times 10^5$, $Sc = 26111$, $D_B = 3.8525 \times 10^{-11}$, $D_T = 8.7252 \times 10^{-12}$, $N_{TBTC} = 0.75495$ and $N_{TBT} = 0.0075495$. The Rayleigh number (Ra_T) and the solutal Rayleigh number (Ra_C) are varied to understand the nanofluid characteristics as well as the heat transfer. The ratio of Ra_T and Ra_C is fixed to 10^2. Most importantly, D_B, D_T,Le, Sc, $N_{TBTC}$and N_{TBT} change according to the particle size, nanoparticle volume fraction and thermophysical properties of base fluid and particle. In the present investigation, the variations of $Ra_T = 10^4 - 10^7$, $Ra_C = 10^2 - 10^5$, $\phi = 0 - 0.05$, $d_p = 1 - 50$ nm, $\varphi = 0^{\circ}$, 9°, 15.75° on streamlines, isotherms, isoconcentrations, local and average Nusselt number for different time steps have been analyzed.

Fig. 3 illustrates the effects of the Rayleigh number and nanoparticle

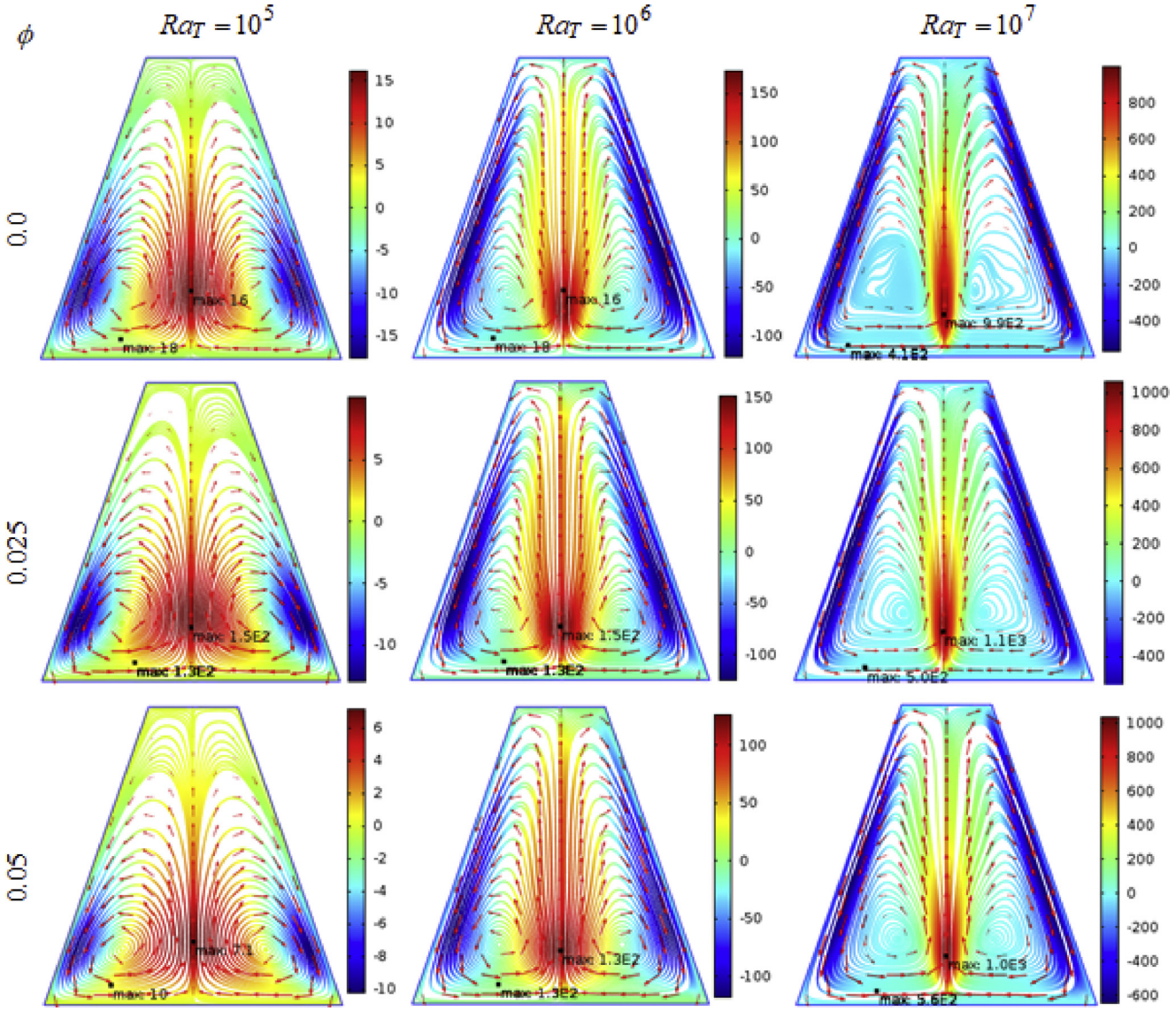

Fig. 3. Streamlines for the nanoparticle volume fraction (ϕ) and thermal Rayleigh number (Ra_T) for the fixed nanoparticle diameter, $d_p = 10$ nm at $\xi = 0.2$.

volume fraction on streamlines. As can be seen that two strongly clockwise and anticlockwise symmetric vortices are significantly rotating in the entire cavity showing the normal nature of convection. A velocity layer is significantly visible between the two vortices in the middle of the cavity for all cases. Also, two velocity boundary layers are formed remarkably on the sloping boundaries. For the lower thermal Rayleigh number ($Ra_T = 10^5$), streamlines are feeble and not that much vigorous. Streamlines have a tendency to be elongated horizontally which is an indication of the conductive mode of energy production in the enclosure. The two centers of the vortices are appeared near the inclined colder walls of the cavity due to a strong temperature gradient on that part. Maximum velocities for *X* and *Y*-directions are not significant that means solids of the fluid is deficient in fluid motion activities. The velocity boundary layers are not visible on the entire colder walls, only formed near the corners of the cavity due to the formation of temperature gradient only on that portion. Because of slow flow, the densities of the streamlines are very high as well as uniform in this case. These are due to the lower temperature differences which result in the lower buoyancy force in an entire nanofluid. As the thermal Rayleigh number enhances ($Ra_T = 10^7$), the fluid motion increases, the temperature gradient forms on the entire nanofluid as well as the boundaries of the vessel, the streamlines become stronger and elongates vertically, maximum values of the velocities enhance significantly and the densities of streamlines noticeably reduced. The streamlines nonuniformly distort and some streamlines cluster on each other. The thickness of the velocity boundary layers on the colder walls increases. The cores of the convection cells have a tendency to come across in the middle of the vortices and they look like two eyes of an owl. The thickness of the resultant velocity layer between the two big vortices decreases in this case whereas very thin three parallel layers in the middle of the cavity are formed for higher thermal Rayleigh number indicates a strong convection cell rotate in the entire vessel which drives the higher heat transfer in the application. These are due to the results of higher temperature differences within nanofluid which create higher buoyancy force in the cavity. The fluid motion at the corners of the geometry is high for a higher Rayleigh number because of temperature gradient forms on the angle between two walls. Fig. 3 also shows noticeable effects of nanoparticle volume fraction on streamlines. The effects of nanoparticle volume fraction on fluid flow

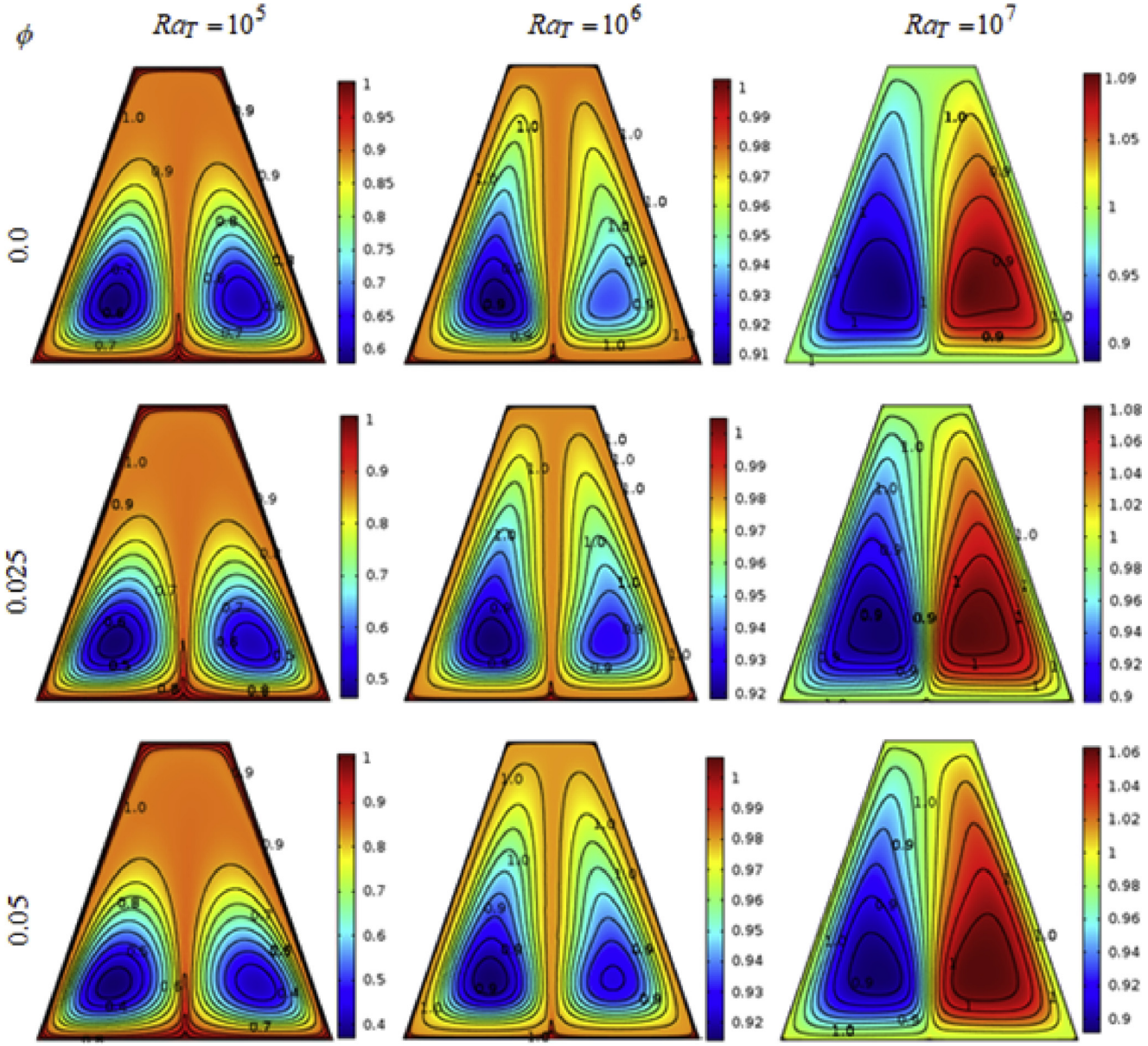

Fig. 4. Isoconcentrations for several nanoparticle volume fractions and thermal Rayleigh number for fixed value of the nanoparticle diameter, $d_p = 10$ nm at $\xi = 0.2$.

are connected with the state of buoyancy force. Without nanoparticle in the base fluid, the streamlines are expansive and loosely connected with each other. The convective cells have a tendency to move horizontally towards colder boundaries speedily due to results of diminutive rotations of strong vortices. Also, for lower Rayleigh number ($Ra_T = 10^5$), the densities of streamlines of base fluid are high at the cores of the vortices near a lower boundary of the cavity whereas for $Ra_T = 10^7$, the convective cells of the vortices are not that much high and they are parallel to the boundaries of the vessel. The cores of the vortices are conspicuously distorted and velocity layers are formed significantly near at all boundaries in this case. For nanofluid, the streamlines have a tendency to be compressed to the middle of the cavity throughout the cases due to higher densities of nanoparticles. The thickness of the boundary layers of nanofluid is less than that of the base fluid. As nanoparticle volume fraction increases, boundary layers thickness decreases, densities and strength of the streamlines increases due to the random motions of nanoparticle which enhances rotational movements in convective cells. The maximum velocities of nanofluid increases for a certain level of nanoparticle volume fraction and thermal Rayleigh number. As we have seen that for, $Ra_T = 10^5$, the maximum velocities increase up to 2.5% nanoparticle volume fraction in the mixture and after that, they decrease. However, $Ra_T = 10^7$, maximum velocity increases up to 5% nanoparticle volume fraction. These indicate that the adjustment between the buoyancy force and nanoparticle volume fraction is highly required in the application.

Fig. 4 represents isoconcentrations for several nanoparticle volume fractions and thermal Rayleigh number. The level of isoconcentrations represents the state of the uniformities of nanoparticles in the mixture and this will allow us to understand the stability of solid particle. As can be seen that two oppositely rotating symmetric loops of isoconcentration are very active in the vessel throughout the cases. The loops of isoconcentration are almost similar to that of the streamlines of the flow. This indicates that the fluid flow in this geometrical shape is optimal in the heat transfer application. The level of isoconcentration of nanofluid is higher than that of the base fluid. This is due to superfluous random motions of nanoparticles in water. Also, the cells of active loops for base fluid are flourishing and dispersive in the entire cavity whereas for nanofluid they slightly compress each other due to an increased density of the mixture. For lower Rayleigh number, the loops of isoconcentration elongate vertically for base fluid whereas the cells in all loops for nanofluid distribute horizontally. This is due to the lower temperature differences but for a higher density of nanofluid. The cells density in each

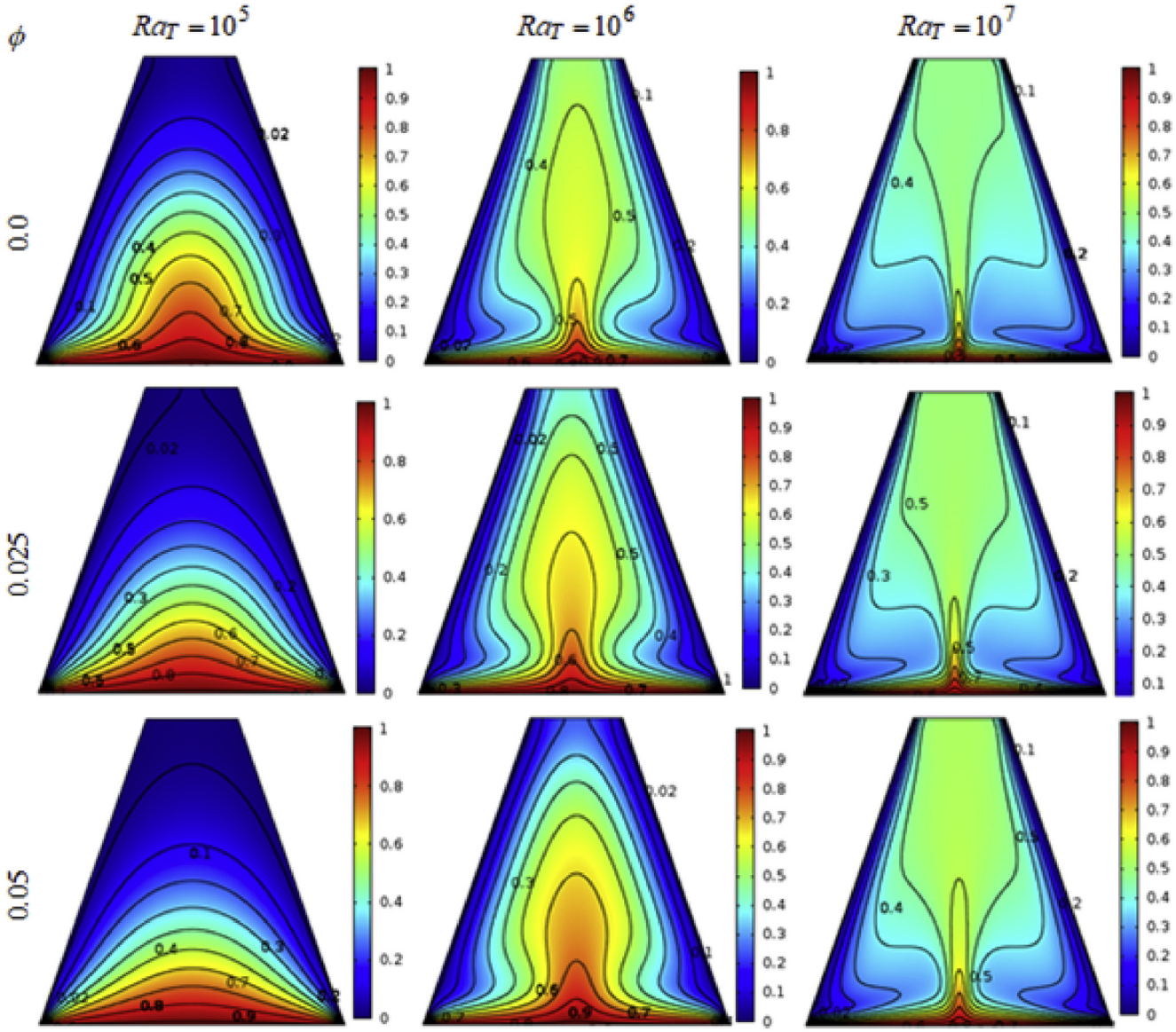

Fig. 5. Isotherm for several nanoparticle volume fractions and thermal Rayleigh number for fixed $d_p = 10$ nm at $\xi = 0.2$.

loop of isoconcentrations for nanofluid significantly higher than that of base fluid because nanoparticle takes heat energy from the heated bottom wall and randomly migrates in the entire cavity. As the nanoparticle volume fraction increases, the levels of concentration, cells densities, and strength of isoconcentration loops increase due to nanoparticles random and thermophoretic diffusive nature. The effects of this phenomenon are increased remarkably for higher buoyancy force. It is an important point to note that for a lower Rayleigh number loops of isoconcentrations are compressed to the base wall and not spread in the entire enclosure which indicates that the conduction mode of heat transfer dominates in the enclosure. On the other hand, for the higher Rayleigh number isoconcentration cells distribute in the entire enclosure. The cells densities of each loop are significantly higher than that of the lower Rayleigh number. This indicates that convective cells of the isoconcentration dominate in this case.

The effect of solid volume fraction on isotherms for selected values of Ra_T at $\xi = 1$ is displayed in Fig. 5. The results of this figure will give us insights regarding characteristics of energy diffusion within the fluid-filled cavity. Also, the mode of heat transfer can be identified in different locations of the domain in this case. Each line of isotherm within the cavity represents heat transfer capabilities from the bottom wall to the sloping walls through the fluid. The fluid takes heat from the heated wall, then carries it towards the colder wall where particles of fluid enhance heat transfer rate on colder walls. As can be seen from the figure that nanoparticle volume fraction and buoyancy parameter significantly affects isotherms. For a lower value of thermal Rayleigh number, ($Ra_T = 10^5$), isotheres did not significantly influence near heated and colder walls. Only in the middle of the cavity, they are normally distributed and shows convection mode of heat transfer where little contorted cells visible. There exist poor isotherms leveling in the entire enclosure except near the heated wall at which isotherm lines parallel to each other which indicates that conduction mode of heat transfer governs at a heated wall. As nanoparticle volume fraction increases, isotherms compress to each other and tend to come across slowly towards the heated wall. These are due to the lesser temperature gradient and higher temperature differences within the fluid neighboring the heated wall that produces higher conduction cells on that portion and convection cells in the middle of the vessel. For $Ra_T = 10^6$, isotherms are distorted in the middle of the cavity and parallel distributions of isotherm are seen near the colder walls. Isotherms are looking like shining candlelight shaped in the middle of the vessel which indicates convection mode of heat transfer dominates in this case. As nanoparticle volume fraction increases, in this case, isotherms are highly compacted and curved in the middle and coming close to the lower wall due to the

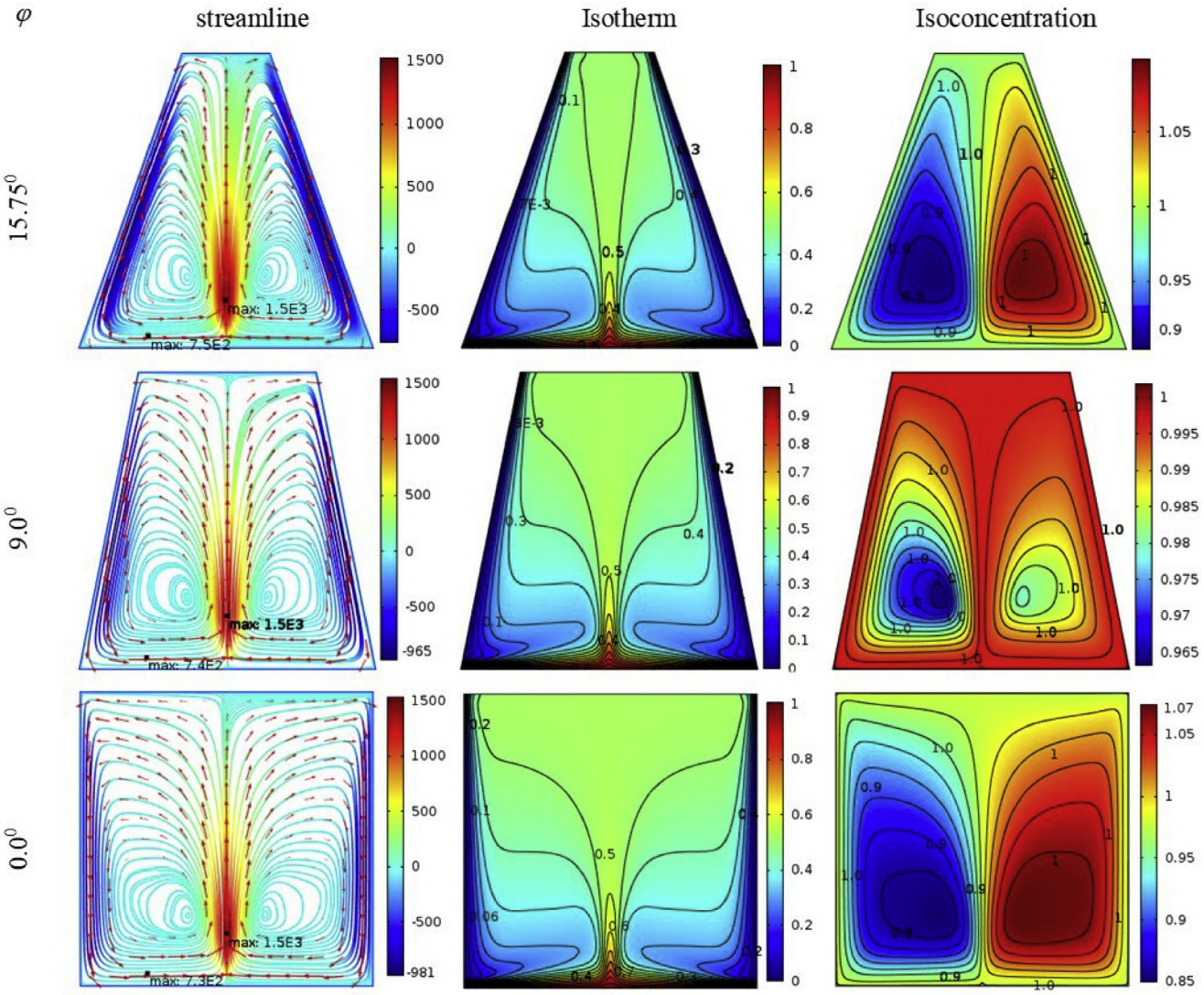

Fig. 6. Vertical walls effects on flow (1st column), thermal (2nd column) and concentration (3rd column) fields for fixed $d_p = 10$ nm, $Ra_T = 1.72 \times 10^7$, $\phi = 0.05$ at $\xi = 0.2$.

addition of more nanoparticles with base fluid. This indicates a higher convection mode of heat transfer happens in the middle. As thermal Rayleigh number increases, the distortions and levels of isotherms increase which yields convection mode of heat transfer significantly increases. For $Ra_T = 10^7$, the thermal boundary layer of isotherms formed on the colder walls designates higher conduction mode of heat transfer. The isotherms noticeably bloom at the heated wall indicates convection mode of heat transfer dominates. It is important to observe that only convective isotherm cells exist in the middle of the vessel. As nanoparticle volume fraction increases in this situation, isotherms distorts to a greater extent. Also, the thickness of the boundary layers decreases as a result of increased migrations and interactions of solid nanoparticles for advanced temperature variances. Henceforth, it can be settled that in the whole vessel apart from near the leaning partitions and an insulated upper barricade, isotherms deformed severely that specifies advanced convection mode of heat transfers. Also, as solid particle rises in the fluid, the upturn curves of temperature traced in the entire cavity. Hence, the higher heat transfer can be found at the higher nanoparticle volume fraction and thermal Rayleigh number.

The effects of three sloping angles ($\varphi = 15.75^{\circ}$,$\varphi = 9^{\circ}$ $\varphi = 0^{\circ}$) on streamlines, isotherms, and isoconcentrations have been depicted in Fig. 6. As can be seen that streamlines, isotherms, and isoconcentrations are significantly influenced by the sloping angles. The symmetric pattern of isotherms, streamlines and isoconcentrations occur inside the cavity for three distinct sloping angles. These happen because the quadrilateral vessel is symmetric with a uniform thermal boundary condition acts on the bottom wall and higher buoyancy force acts against gravity. Also, thermal diffusions of nanoparticles happen uniformly in the entire cavity. The two opposite rotational vortices strongly visible throughout the cases. Two oppositely rotational vortices are strongly visible throughout the cases. The cores of the streamlines are looked like owls eyes. The velocity layers are significantly pronounced on the vertical walls as well as in the middle of two vortices. However, there are significant distinctions among three streamlines in three different geometries. The velocity boundary layer thickness as well as the layers in the middle vortices, streamlines densities and cores areas of two vortices inside the quadrilateral having, $\varphi = 15.75^{\circ}$ are pointedly higher than that of other quadrilaterals having $\varphi = 9^{\circ}$ and $\varphi = 0^{\circ}$ respectively. It is important to note that velocities in X-direction are same throughout the cases whereas velocity in Y direction within the cavity having an angle $\varphi = 15.75^{\circ}$ is higher than that of the cavity having angles $\varphi = 9^{\circ}$ and $\varphi = 0^{\circ}$ respectively. These are due to the fact that the two higher tended colder walls are closed to a heated wall which can take heat hastily. Also, the solid nanoparticle can rapidly migrate from the heated wall to the colder walls and after that can come back quickly in the middle portion of the vessel.

This figure also depicts the changes of isotherms for three different sloping angles ($\varphi = 15.75^{\circ}$, $\varphi = 9^{\circ}$ and $\varphi = 0^{\circ}$). As we have seen that isotherms are strong, contorted and spread in the entire geometry throughout the cases. However, little distinctions among them can be observed. The isotherms of the trapezoidal cavities are slightly stronger and more convoluted than that of the square geometry ($\varphi = 0^{\circ}$). The

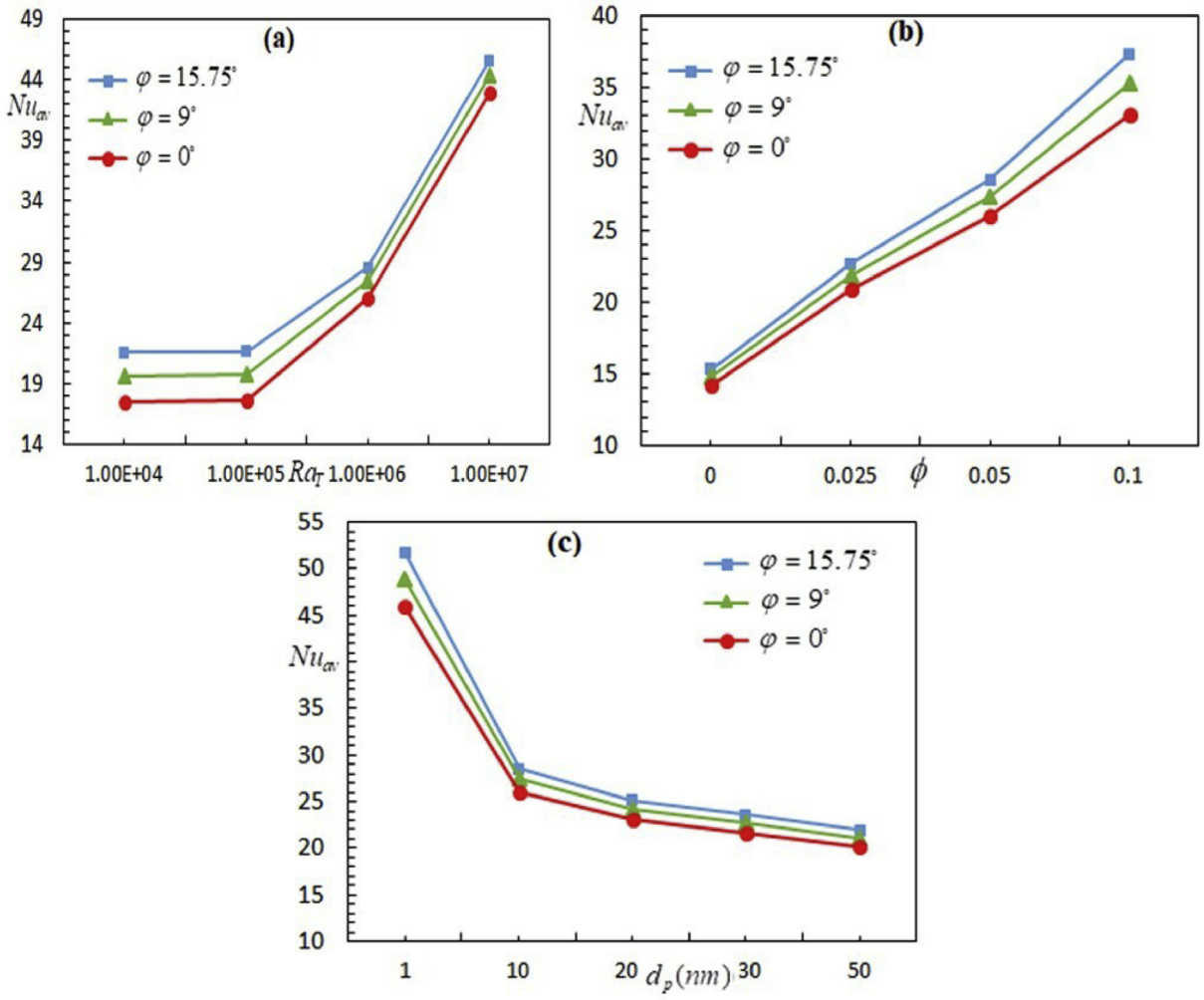

Fig. 7. Effects of $\varphi = 15.75^{\circ}$, $\varphi = 9^{\circ}$ and $\varphi = 0^{\circ}$ in terms of Nu_{av} for (a) Rayleigh number (b) nanoparticle volume fraction and (c) nanoparticle diameter for fixed $d_p =$ 10 nm, $Ra_T = 1.72 \times 10^7$, $\phi = 0.05$ at $\xi = 0.2$.

convective cells for case-1 ($\varphi = 15.75^{\circ}$) are higher than that of case-2 ($\varphi = 9^{\circ}$). The thermal boundary layer thickness in the geometry for case-3 ($\varphi = 15.75^{\circ}$) is less than that of the other two cases. This happens because particles can take heat from the heated wall and immediately migrates to the colder walls rather than staying in the middle. These indicate that higher heat transfer happens in the quadrilateral vessel having a higher possible sloping angle (φ). Also, two strong loops of isoconcentrations are spread in the entire quadrilateral vessel in all cases. Surprisingly, slightly more uniformities of nanoparticles in the base fluid and firmest isoconcentrations are observed for case-2. The densities and levels of the convective cell of isoconcentrations are higher than that of the other two cases. This indicates that spacious geometry with slanting colder walls can determine the higher stabilized condition in the heat transfer application.

The effects of three sloping angels ($\varphi = 15.75^{\circ}$, $\varphi = 9^{\circ}$ and $\varphi = 0^{\circ}$) in terms of average Nusselt number are described in Fig. 7. This illustrates heat transfer rate on the heated bottom wall of the cavity for different (a) thermal Rayleigh number (b) nanoparticle volume fraction and (c) nanoparticle diameter when $d_p = 10$ nm, $Ra_T = 1.72 \times 10^7$, $\phi = 0.05$. We have seen that the average Nusselt number is significantly enhanced if the sloping angle, thermal Rayleigh number, nanoparticle volume fraction are increased and nanoparticle diameter is decreased. From Fig. 7 (a), we have seen that as the angle, φ increases, the average heat transfer increases. This enhancement in heat transfer is significantly higher for the lower thermal Rayleigh number than that of the higher thermal Rayleigh number. As thermal Rayleigh number goes to a pointedly high value, the average Nusselt number on the heated wall tends to meet at a certain point. Average Nusselt number is almost similar for both $Ra_T = 10^5$ and $Ra_T = 10^4$ in all circumstances which indicate a pure conduction mode of heat transfer. Importantly, rapid heat transfer enhancement starts from $Ra_T = 10^5$ in all cases and this represents a critical thermal Rayleigh number of the current system. Fig. 7(b) shows augmentation in heat transfer for three different sloping angles (φ). It observes that the heat transfer improvement is not that much significant for the base fluid whereas remarkably higher heat transfer increment occurs for nanofluid. Also, as nanoparticle volume fraction increases in nanofluid, heat transfer increases promptly for the vessel having $\varphi = 15.75^{\circ}$ whereas it rises regularly for a square enclosure where $\varphi = 0^{\circ}$. The effects of nanoparticle size in terms of average Nusselt number in three different sloping angles of the vessel are depicted in Fig. 7(c). As can be seen that a rapid decrease in heat transfer is found for the particle size 1 nm to 10 nm and after that, a gradual decrease is noticed for all sloping angles. The declined in heat transfer rate happens significantly for the trapezoidal vessel having ($\varphi = 15.75^{\circ}$and $\varphi = 9^{\circ}$) than that of a square cavity where $\varphi = 0^{\circ}$. So, it can be concluded that the nanoparticle size and geometrical shape of heat transfer objects matter outstandingly in

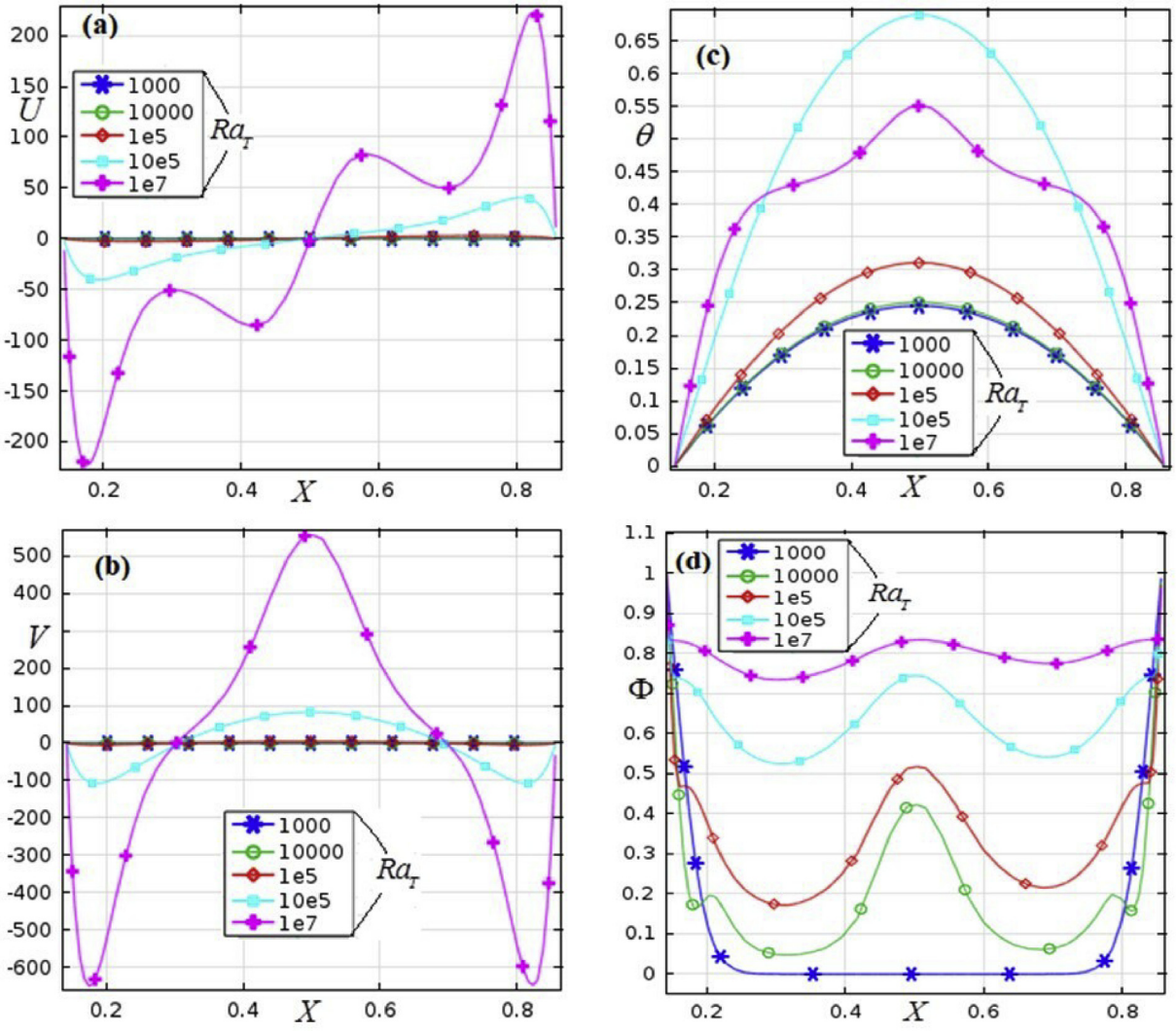

Fig. 8. (a) velocity in X-direction (b) velocity in Y-direction (c) temperature, and (d) concentration profile on the cut-line at $Y = 0.4$, $0.14 \leq X \leq 0.86$ for fixed $d_p = 10$ nm, $Ra_T = 10^7$, $\phi = 0.05$ at $\xi = 0.2$.

the heat transfer application.

The velocity in X-direction, velocity in Y-direction, temperature and concentration profile at $Y = 0.4$, $0.14 \leq X \leq 0.86$ of trapezoidal cavity having $\varphi = 15.75^{\circ}$ is shown in Fig. 8 (a)–(d) respectively. From Fig. 8(a), we have seen that the distribution of U-velocity is almost zero on the cut-line for lower thermal Rayleigh number, $Ra_T = 10^3 - 10^5$. The positive and negative values of U-velocity are found for $Ra_T = 10^6 - 10^7$ and the U-velocity increases at interval $0.45 \leq X \leq 0.86$ and decreases at $0.14 \leq X \leq 0.45$ significantly for $Ra_T = 10^6 - 10^7$ whereas it intersects at $X = 0.45$, $Y = 0.4$. The maximum and minimum values of U-velocity are found near at the right and left walls of the cavity respectively in this case. The maximum and minimum values of U-velocity increase rapidly as the thermal Rayleigh number enhances. Interestingly, similar results are found for V-velocity for lower Rayleigh number ($Ra_T = 10^3 - 10^5$) but for a higher Rayleigh number, the patterns and distributions of V-velocity are distinct than that of U-velocity shown in Fig. 8(b). We have seen that a positive downward parabolic profile on $0.3 \leq X \leq 0.7$ and two negative upward parabolic profile of V-velocity along with two intersecting points on the cut-line at $X = 0.3$ and $X = 0.7$ are observed. For the higher Rayleigh number, two similar minimum values of V–velocity have been found on the cut-line at which the minimum and maximum of U-velocity are found whereas maximum value of V-velocity is found at which U-velocity is intersected. Also, V-velocity distribution expanses sharply in this case. Temperature profiles for various thermal Rayleigh number shown in Fig. 8(c).

The simultaneous semicircular shaped of temperature profiles are observed for $Ra_T = 10^3 - 10^4$. Interestingly, the temperature distributions are increased significantly for $Ra_T = 10^4 - 10^6$. Also, maximum temperature is found at the middle of the cut-line for $Ra_T = 10^6$ which indicates that thermal diffusion of nanoparticles is maximum at that point. For $Ra_T = 10^7$, temperature profile is distorted and declined rapidly in the middle, have a tendency to be distributed evenly and enhanced at both sides of the cut-line than that of $Ra_T = 10^6$ which shows a uniform temperature distribution. This is due to the higher temperature differences in the entire cavity that strengthen the buoyancy force which acts against the gravity. The thermal diffusions of solid nanoparticles occur in the entire vessel as well, which makes even temperature distribution. The concentration profile has been shown in Fig. 8(d), and depicted that as thermal Rayleigh number enhances, concentration profiles and uniformity of concentration levels enhance meaningfully in the whole cavity. For $Ra_T = 10^3$, higher concentration notices at the left and right sides of the cut-line whereas in the middle it is almost zero whereas concentration profile and levels are fluctuated for $Ra_T = 10^3 - 10^6$. Henceforth, uniform nanoparticle distributions with nanofluid happens at higher Rayleigh number.

The time evolution for a steady-state solution has been illustrated by Fig. 9(a)–(d). In this section, we have investigated time evolution for a steady-state solution for different parameters entered into the problem.

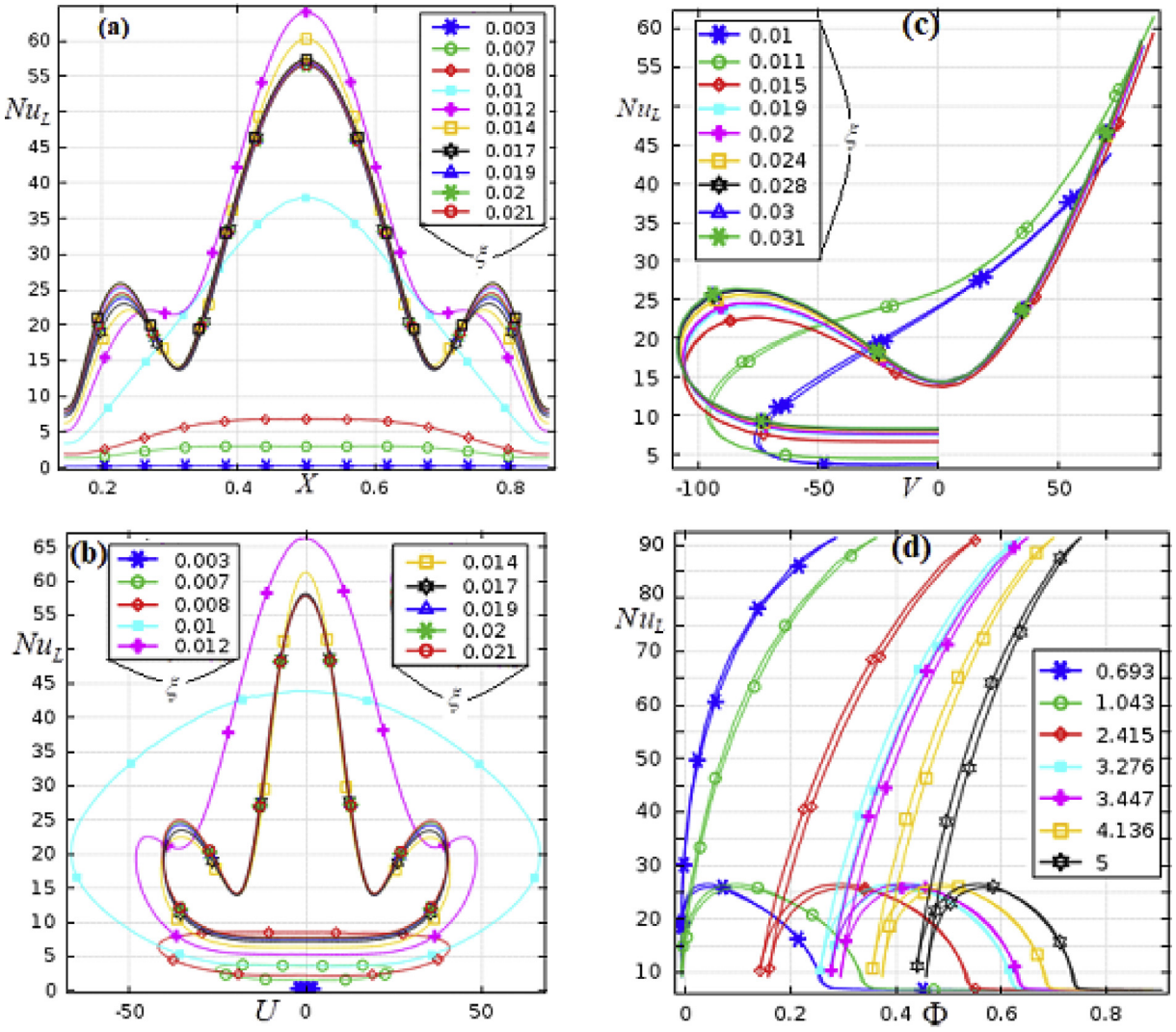

Fig. 9. Local Nusselt number versus (a) $Y = 0.4$, $0.14 \leq X \leq 0.86$ (b) U-velocity (c) V-velocity and (d) concentration, C for fixed $d_p = 10$ nm, $Ra_T = 10^6$, $\phi = 0.05$.

Note: the analysis of stability or instability for various ranges of parameters within the prescribed domain have not taken part in the current result and discussion. Here, Fig. 9(a)–(d) represents local Nusselt number distribution for natural values of X (within the domain), velocity in X-direction, velocity in Y-direction, temperature, and concentration for numerous time steps on the cut-line at $Y = 0.4$, $0.14 \leq X \leq 0.86$. The pattern and distributions of local Nusselt number showed significant dissimilarities because of the different contributions from each variable. Concomitantly, the change in heat transfer has a significant dependence compared to the natural phenomenon on time, thus the local Nusselt number has been significantly influenced by several time steps. The local Nusselt number versus X values of the cut-line for different times has been depicted in Fig. 9(a). Where the heat transfer distribution increases normally for the initial periods of time, then starts to decrease with contortions and it becomes steady after a certain time. The steady-state local Nusselt number has been obtained at $\xi = 0.021$ where the heat transfer distributions are symmetric on the cut-line but overlapped each other after a certain period of time. The maximum heat transfer obtained at $X = 0.5$ and minimum heat transfer occurred at the left and right side of the line because the cavity's slanting walls influence nanoparticles to diffuse in the middle.

For different time steps, the heat transfer distribution versus velocity in X direction has been represented in Fig. 9(b). We have seen equal positive and negative distributions of U-velocity on the cut-line which indicate identical symmetric clockwise and anticlockwise rotations of vortices in the cavity for heat transfer enhancement. The maximum heat transfer has been noticed at $U = 0$. Elliptic shaped of heat transfer distributions are observed for $\xi \in [0.003, 0.01]$. As time goes on, interestingly symmetric shaped of heat transfer disseminations has been contributed for U-velocity. After $\xi = 0.017$, the heat transfer distributions have coincided for the rest of the time steps which means that steady solution occurred for U-velocity at this time period. Fig. 9(c) represents the local Nusselt number distributions versus V-velocity. Overlapped and asymmetric heat transfer distribution have been observed for negative and positive V-velocity for various time steps. As time is increased, the heat transfer distributions are increased. The heat transfer distribution looks like a loop for negative V-velocity whereas it decreases significantly and almost an increasing line for positive V-velocity.

The maximum heat transfer has been noticed for a higher positive value of V-velocity. The steady state heat transfer distribution occurs for the contribution of V-velocity at $\xi = 0.028$. Fig. 9 (d) represents time effects on heat transfer distribution for concentration on the cut-line. As can be seen that the heat transfer distribution for various concentration levels has been changed over the periods of time. The higher heat transfer has been noticed at the higher concentration levels. Initially, local

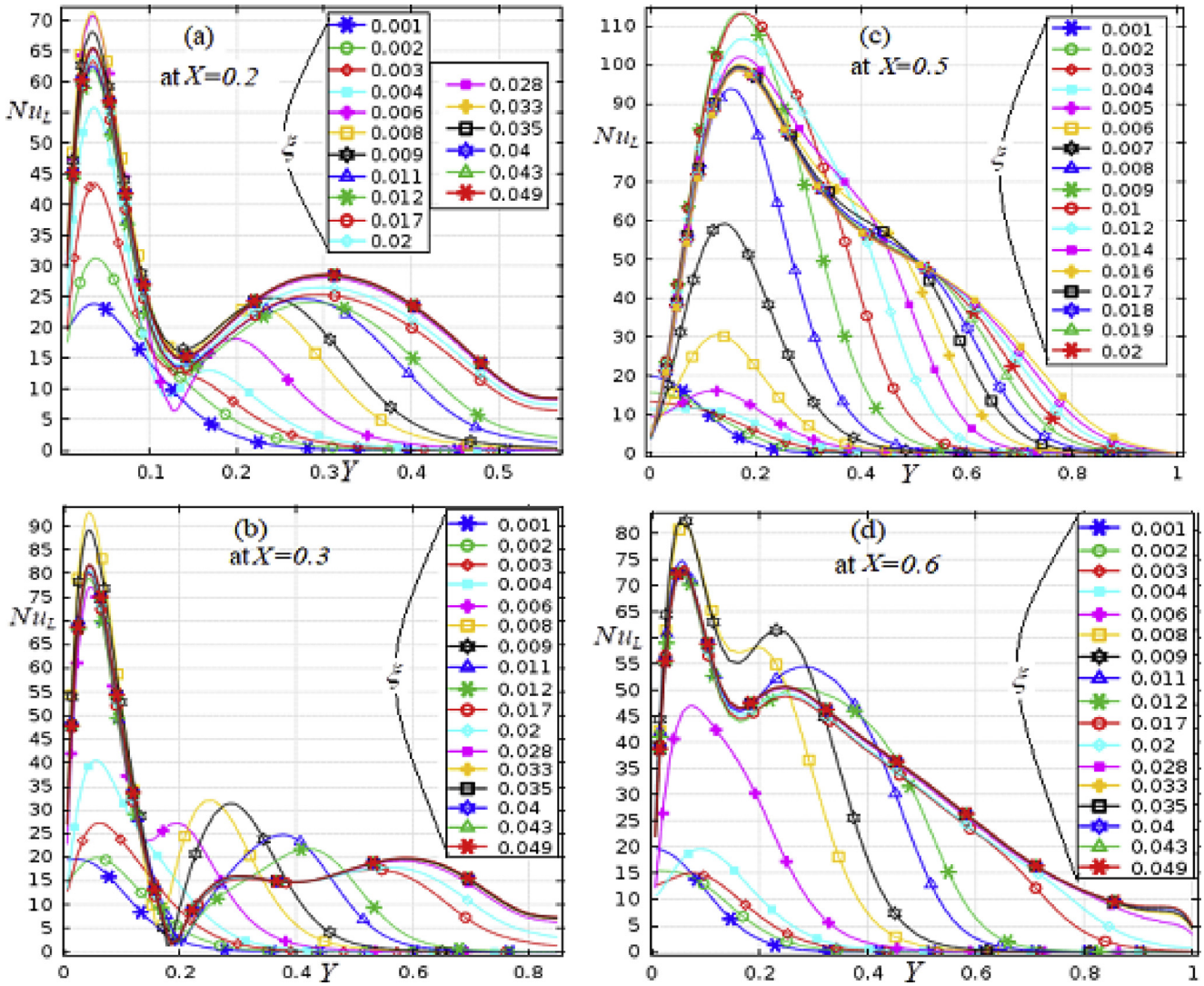

Fig. 10. Local Nusselt number distribution on the vertical cut-lines of the trapezoidal cavity for several time steps at (a) $X = 0.2$, (b) $X = 0.3$ (c) $X = 0.5$, and (d) $X = 0.6$ when $d_p = 10nm$, $\phi = 0.05$, $Ra_T = 10^6$.

Nusselt number distributions have been found at the low concentration level. As time increases, the local Nusselt number distributions have been shifted at higher concentration levels. So, steady state and higher heat transfer distribution can be obtained after a certain time period.

The time evolutions in terms of local Nusselt number distributions on the numerous vertical cut-lines have been shown in Fig. 10 (a)–(d). As can be seen that time steps significantly affects the local Nusselt number distribution. The pattern and distributions of local Nusselt number on different vertical cut-lines are dissimilar at different positions in the cavity. Initially, local Nusselt number distributes on the lower portion of the cut-line and as time goes on, it propagates in the entire line throughout the cases. The higher value of local Nusselt number has been observed at the lower side of the cut-line because of the heated wall. Fig. 10(a) shows local Nusselt number distributions on a vertical cut-line at $X = 0.2$ for different time steps. It is seen that as time step increases, the local Nusselt number distributions rise sharply with fluctuating. After a certain time, it reaches a stable state with little change. The steady state condition of local Nusselt number occurs at $\xi = 0.028$ in this case. The maximum values of local Nusselt number for different time steps have been obtained at $Y = 0.03$. The local Nusselt number distributions (Nu_L) for various time steps drop down sharply from their maximum values at $Y = 0.12$. Then heat transfer distributions look like a downward parabola shaped where distributive lines overlap each other. Fig. 10(b) represents the local Nusselt number (Nu_L) distributions on the line at $X = 0.3$ different time steps. The patterns of Nu_L curves are importantly different than that of the curves at $X = 0.2$. As can be seen that the distributions of local Nusselt number for different time stages have been increased initially and then fluctuated. They are looked like different oceanic waves throughout the time periods. The maximum Nu_L has been found at $Y = 0.08$ for $\xi = 0.008$ and local Nusselt number curve starts increasing from a higher value, reached to a peak, then drops down sharply to a lower value and then again distribute in a wavy pattern. These patterns of heat transfer distribution within a vessel indicate that the molecules, as well as nanoparticles random motions and thermophoretic behaviors, contribute to heat transfer enhancement. The steady state solution, in this case, occurred at $\xi = 0.04$. Instead of wavy shaped, almost downward parabolic local Nusselt number distributions have been noticed for numerous time steps on a vertical cut-line at $X = 0.5$ which is portrayed in Fig. 10 (c). In addition, the heat transfer disseminations have been fluctuated and overlapped for a certain time step and then they become steady for the rest of the time. The steady state solution in terms of Nu_L has been ensued early at $\xi = 0.027$ than that of other cases. Among the maximum values of local Nusselt number in various positions within the cavity, the highest maximum value has been obtained in this case because higher thermal diffusions happen in the middle of the cavity. Fig. 10 (d) represents local Nusselt number distributions at $X = 0.6$. It is observed that the Nu_L distributions are similar for the initial time steps with that of the distributions at $X = 0.5$. As time increases, the Nu_L distributions reach to a peak and then fluctuates. After a certain time step, the Nu_L distributions drop down sharply at $Y = 0.18$. The steady state solution has been attained at $\xi = 0.035$ in this case.

5. Conclusions

In the present article, the natural convective copper-oxide water nanofluid flow and heat transfer within the quadrilateral vessel using a dynamic model has been investigated numerically. The flow patterns, thermal fields, concentration levels of the nanofluid and base fluid, impacts of variables for different relatable parameters and effects of sloping angles of the vessel are investigated. The central results of the investigation can be summarized as:

(1) A trapezoidal cavity having a possible higher sloping angle exhibits higher heat transfer.
(2) Higher heat transfer distribution has been obtained at higher thermal Rayleigh number and nanoparticle volume fraction.
(3) For higher nanoparticle volume fraction in the solution, higher thermal Rayleigh number is required.
(4) Adjustment between nanoparticle volume fraction and the buoyancy force has been highly required to find an optimum nanofluid flow.
(5) As nanoparticle volume fraction and thermal Rayleigh number increases and particle diameter decreases, the mean heat transfer increases significantly for a trapezoidal cavity having higher slopping angle.
(6) 10^5 is the critical thermal Rayleigh number of the present problem.
(7) Symmetric distribution of velocity, temperature and concentration profiles within the cavity have been obtained at the higher Rayleigh number.
(8) The local Nusselt number dissemination on the horizontal cut-line are symmetric within the cavity whereas the asymmetric distribution of local Nusselt number has been found on the vertical cut-line of the cavity.
(9) The steady-state solution of the problem occurs at different time steps and it depends on the particular parameter settings and geometrical space.

Declarations

Author contribution statement

M. J. Uddin: Conceived and designed the experiments; Performed the experiments; Analyzed and interpreted the data; Contributed reagents, materials, analysis tools or data; Wrote the paper.

S. K. Rasel: Performed the experiments; Analyzed and interpreted the data; Contributed reagents, materials, analysis tools or data; Wrote the paper.

Funding statement

This research did not receive any specific grant from funding agencies in the public, commercial, or not-for-profit sectors.

Competing interest statement

The authors declare no conflict of interest.

Additional information

No additional information is available for this paper.

Acknowledgments

The authors are thankful to the unknown reviewer's useful comments and recommendations for the further development of the article.

References

[1] M.J. Uddin, K.S. Al Kalbani, M.M. Rahman, M.S. Alam, N. Al-Salti, I. Eltayeb, Fundamentals of nanofluids: evolution, applications and new theory, Int. J. Biomath. Syst. Biol. 2 (1) (2016) 1–32.
[2] S.A.M. Mehryan, F.M. Kashkooli, M. Ghalambaz, A.J. Chamkha, Free convection of hybrid Al2O3-Cu water nanofluid in a differentially heated porous cavity, Adv. Powder Technol. 28 (9) (2017) 2295–2305.
[3] A.J. Chamkha, S. Sazegar, E. Jamesahar, M. Ghalambaz, Thermal non-equilibrium heat transfer modeling of hybrid nanofluids in a structure composed of the layers of solid and porous media and free nanofluids, Energies 12 (3) (2019) 541.
[4] S.A.M. Mehryan, E. Izadpanahi, M. Ghalambaz, A.J. Chamkha, Mixed convection flow caused by an oscillating cylinder in a square cavity filled with Cu–Al_2O_3/water hybrid nanofluid, J. Therm. Anal. Calorim. (2019) 1–18.
[5] A. Shenoy, M. Sheremet, I. Pop, Convective Flow and Heat Transfer from Wavy Surfaces: Viscous Fluids, Porous media, and Nanofluids, CRC Press, 2016.
[6] O. Mahian, A. Kianifar, S.A. Kalogirou, I. Pop, S. Wongwises, A review of the applications of nanofluids in solar energy, Int. J. Heat Mass Transf. 57 (2) (2013) 582–594.

[7] O. Mahian, L. Kolsi, M. Amani, P. Estellé, G. Ahmadi, C. Kleinstreuer, et al., Recent Advances in Modeling and Simulation of Nanofluid Flows-Part II: Applications, Physics reports, 2018.
[8] S.K. Das, S.U. Choi, W. Yu, T. Pradeep, Nanofluids: Science and Technology, John Wiley & Sons, 2007.
[9] W.J. Minkowycz, E.M. Sparrow, J.P. Abraham, Nanoparticle Heat Transfer and Fluid Flow, CRC press, 2016.
[10] O. Mahian, L. Kolsi, M. Amani, P. Estellé, G. Ahmadi, C. Kleinstreuer, et al., Recent Advances in Modeling and Simulation of Nanofluid Flows-Part I: Fundamental and Theory, Physics reports, 2018.
[11] H. Saleh, R. Roslan, I. Hashim, Natural convection heat transfer in a nanofluid-filled trapezoidal enclosure, Int. J. Heat Mass Transf. 54 (1–3) (2011) 194–201.
[12] S. Soleimani, M. Sheikholeslami, D.D. Ganji, M. Gorji-Bandpay, Natural convection heat transfer in a nanofluid filled semi-annulus enclosure, Int. Commun. Heat Mass Transf. 39 (4) (2012) 565–574.
[13] R. Roslan, H. Saleh, I. Hashim, Buoyancy-driven heat transfer in nanofluid-filled trapezoidal enclosure with variable thermal conductivity and viscosity, Numer. Heat Tran. Part A Appl. 60 (10) (2011) 867–882.
[14] A.H. Mahmoudi, I. Pop, M. Shahi, F. Talebi, MHD natural convection and entropy generation in a trapezoidal enclosure using Cu–water nanofluid, Comput. Fluid 72 (2013) 46–62.
[15] R. Nasrin, S. Parvin, Investigation of buoyancy-driven flow and heat transfer in a trapezoidal cavity filled with water–Cu nanofluid, Int. Commun. Heat Mass Transf. 39 (2) (2012) 270–274.
[16] N.S. Bondareva, M.A. Sheremet, I. Pop, Magnetic field effect on the unsteady natural convection in a right-angle trapezoidal cavity filled with a nanofluid: Buongiorno's mathematical model, Int. J. Numer. Methods Heat Fluid Flow 25 (8) (2015) 1924–1946.
[17] A. Aghaei, H. Khorasanizadeh, G. Sheikhzadeh, M. Abbaszadeh, Numerical study of magnetic field on mixed convection and entropy generation of nanofluid in a trapezoidal enclosure, J. Magn. Magn. Mater. 403 (2016) 133–145.
[18] F. Selimefendigil, H.F. Öztop, N. Abu-Hamdeh, Natural convection and entropy generation in nanofluid filled entrapped trapezoidal cavities under the influence of magnetic field, Entropy 18 (2) (2016) 43.
[19] H. Alipour, A. Karimipour, M.R. Safaei, D.T. Semiromi, O.A. Akbari, Influence of T-semi attached rib on turbulent flow and heat transfer parameters of a silver-water nanofluid with different volume fractions in a three-dimensional trapezoidal microchannel, Phys. E Low Dimens. Syst. Nanostruct. 88 (2017) 60–76.
[20] M.H. Esfe, A.A.A. Arani, W.M. Yan, H. Ehteram, A. Aghaie, M. Afrand, Natural convection in a trapezoidal enclosure filled with carbon nanotube–EG–water nanofluid, Int. J. Heat Mass Transf. 92 (2016) 76–82.
[21] V.M. Job, S.R. Gunakala, Unsteady MHD free convection nanofluid flows within a wavy trapezoidal enclosure with viscous and Joule dissipation effects, Numer. Heat Tran. Part A Applications 69 (4) (2016) 421–443.
[22] V.M. Job, S.R. Gunakala, B.R. Kumar, R. Sivaraj, Time-dependent hydromagnetic free convection nanofluid flows within a wavy trapezoidal enclosure, Appl. Therm. Eng. 115 (2017) 363–377.
[23] A. Arefmanesh, A. Aghaei, H. Ehteram, Mixed convection heat transfer in a CuO–water filled trapezoidal enclosure, effects of various constant and variable properties of the nanofluid, Appl. Math. Model. 40 (2) (2016) 815–831.
[24] F. Selimefendigil, H.F. Öztop, Numerical study of MHD mixed convection in a nanofluid filled lid driven square enclosure with a rotating cylinder, Int. J. Heat Mass Transf. 78 (2014) 741–754.
[25] M.A. Sheremet, T. Groşan, I. Pop, Steady-state free convection in right-angle porous trapezoidal cavity filled by a nanofluid: Buongiorno's mathematical model, Eur. J. Mech. B Fluid 53 (2015) 241–250.
[26] I.V. Miroshnichenko, M.A. Sheremet, H.F. Oztop, K. Al-Salem, MHD natural convection in a partially open trapezoidal cavity filled with a nanofluid, Int. J. Mech. Sci. 119 (2016) 294–302.
[27] S.M. Al-Weheibi, M.M. Rahman, M.S. Alam, K. Vajravelu, Numerical simulation of natural convection heat transfer in a trapezoidal enclosure filled with nanoparticles, Int. J. Mech. Sci. 131 (2017) 599–612.
[28] J. Buongiorno, Convective transport in nanofluids, J. Heat Transf. 128 (3) (2006) 240–250.
[29] M.J. Uddin, M.M. Rahman, Numerical computation of natural convective heat transport within nanofluids filled semi-circular shaped enclosure using nonhomogeneous dynamic model, Therm. Sci. Eng. Prog. 1 (2017) 25–38.
[30] Y. Xuan, Q. Li, W. Hu, Aggregation structure and thermal conductivity of nanofluids, AIChE J. 49 (4) (2003) 1038–1043.
[31] R.K. Tiwari, M.K. Das, Heat transfer augmentation in a two-sided lid-driven differentially heated square cavity utilizing nanofluids, Int. J. Heat Mass Transf. 50 (9-10) (2007) 2002–2018.
[32] M.J. Uddin, M.A. Halim, M. Mohiuddin, Shalauddin, Copper oxide-water nanofluid flow within an annulus shaped cavity: a numerical study on natural convective heat transfer, Ann. Chimie Sci. Matériaux 41 (3-4) (2017) 239–260.
[33] M.J. Uddin, Numerical simulation on free convective heat transfer in a copper-water nanofluid filled semicircular annulus with the magnetic field, Ital. J. Eng. Sci. Tecnic. Ital. 62 (2) (2018) 119–129.
[34] O.C. Zienkiewicz, R.L. Taylor, P. Nithiarasu, The Finite Element Method for Fluid Dynamics, sixth ed., Elsevier, 2005.
[35] R. Codina, Comparison of some finite element methods for solving the diffusion-convection-reaction equation, Comput. Methods Appl. Mech. Eng. 156 (1–4) (1998) 185–210.
[36] M.J. Uddin, M.M. Rahman, Finite element computational procedure for convective flow of nanofluids in an annulus, Therm. Sci. Eng. Prog. 6 (2018) 251–267.
[37] B. Ghasemi, S.M. Aminossadati, A. Raisi, Magnetic field effect on natural convection in a nanofluid-filled square enclosure, Int. J. Therm. Sci. 50 (9) (2011) 1748–1756.
[38] G. de Vahl Davis, Natural convection of air in a square cavity: a bench mark numerical solution, Int. J. Numer. Methods Fluids 3 (3) (1983) 249–264.
[39] D.C. Wan, B.S.V. Patnaik, G.W. Wei, A new benchmark quality solution for the buoyancy-driven cavity by discrete singular convolution, Numer. Heat Tran. Part B: Fundam. 40 (3) (2001) 199–228.
[40] W. Williams, J. Buongiorno, L.W. Hu, Experimental investigation of turbulent convective heat transfer and pressure loss of alumina/water and zirconia/water nanoparticle colloids (nanofluids) in horizontal tubes, J. Heat Transf. 130 (4) (2008), 042412.
[41] F. Garoosi, L. Jahanshaloo, M.M. Rashidi, A. Badakhsh, M.E. Ali, Numerical simulation of natural convection of the nanofluid in heat exchangers using a Buongiorno model, Appl. Math. Comput. 254 (2015) 183–203.
[42] S.J. Kim, I.C. Bang, J. Buongiorno, L.W. Hu, Surface wettability change during pool boiling of nanofluids and its effect on critical heat flux, Int. J. Heat Mass Transf. 50 (19–20) (2007) 4105–4116.
[43] M.J. Uddin, M.M. Rahman, M.S. Alam, Analysis of natural convective heat transport in homocentric annuli containing nanofluids with an oriented magnetic field using nonhomogeneous dynamic model, Neural Comput. Appl. 30 (10) (2018) 3189–3208.
[44] M.J. Uddin, M.S. Alam, N. Al-Salti, M.M. Rahman, Investigations of natural convection heat transfer in nanofluids filled horizontal semicircular-annulus using nonhomogeneous dynamic model, Am. J. Heat Mass Transf. 3 (6) (2016) 425–452.
[45] M.J. Uddin, M.S. Alam, M.M. Rahman, Natural convective heat transfer flow of nanofluids inside a quarter-circular enclosure using nonhomogeneous dynamic model, Arabian J. Sci. Eng. 42 (5) (2017) 1883–1901.
[46] M.J. Uddin, A.F. Hoque, Convective heat transfer flow of nanofluid in an isosceles triangular shaped enclosure with an uneven bottom wall, Chem. Eng. Trans. 66 (2018) 403–408.